

The ANDICAM-SOFI Near-infrared and Optical type Ia Supernova (ASNOS) sample: Description and data release

Kim Phan^{1,2*}, Lluís Galbany^{2,1}, Tomás E. Müller-Bravo^{3,4}, Subhash Bose⁵, Christopher R. Burns⁶, Maximilian D. Stritzinger⁵, Camilla T. G. Sørensen⁵, Chris Ashall⁷, Francisco J. Castander^{2,1}, Cristina Jiménez Palau^{2,1}, Joel Johansson⁸, Joseph P. Anderson⁹, Ken. C. Chambers¹⁰, Mariusz Gromadzki¹¹, Priscila J. Pessi⁸, and Ting-Wan Chen¹²

¹ Institut d'Estudis Espacials de Catalunya (IEEC), E-08034 Barcelona, Spain.

² Institute of Space Sciences (ICE, CSIC), Campus UAB, Carrer de Can Magrans, s/n, E-08193 Barcelona, Spain.

³ School of Physics, Trinity College Dublin, The University of Dublin, Dublin 2, Ireland

⁴ Instituto de Ciencias Exactas y Naturales (ICEN), Universidad Arturo Prat, Chile

⁵ Department of Physics and Astronomy, Aarhus University, Ny Munkegade 120, DK-8000 Aarhus C, Denmark

⁶ Observatories of the Carnegie Institution for Science, 813 Santa Barbara St, Pasadena, CA, 91101, USA

⁷ Institute for Astronomy, University of Hawai'i at Manoa, 2680 Woodlawn Drive, Hawai'i, HI 96822, USA

⁸ Oskar Klein Centre, Department of Physics, Stockholm University, AlbaNova, SE-10691 Stockholm, Sweden

⁹ European Southern Observatory, Alonso de Crdova 3107, Casilla 19 Santiago, Chile

¹⁰ Institute for Astronomy, University of Hawai'i, 2680 Woodlawn Dr., Honolulu, HI 96825

¹¹ Astronomical Observatory, University of Warsaw, Al. Ujazdowskie 4, 00-478 Warszawa, Poland

¹² Graduate Institute of Astronomy, National Central University, 300 Zhongda Road, 32001 Jhongli, Taiwan

Received December 4, 2025; accepted XXX

ABSTRACT

Type Ia supernovae (SNe Ia) provide the most robust means of measuring extragalactic distances. While most of the effort has focused on increasing the number of SNe Ia observed in the optical, near-infrared (NIR) observations remain scarce despite their advantages, that is, reduced dust extinction and a more intrinsic standard candle behavior, requiring little to no empirical corrections. Here, we present ASNOS (ANDICAM-SOFI Near-infrared and Optical type Ia Supernova), a dataset with sample size of 1,482 epochs in the *BVR_{IYJH}* filters from the ANDICAM instrument on the 1.3-meter SMARTS telescope at Cerro Tololo Inter-American Observatory, along with 125 *JHK* epochs from the SOFI instrument on the 3.58-meter New Technology Telescope on the La Silla Observatory. Additionally, we incorporate optical forced photometry from the Zwicky Transient Facility and the Asteroid Terrestrial-impact Last Alert System. The sample comprises 41 SNe Ia in total, including 29 normal events, eight 1991T-like objects, and four peculiar subtypes, all located at redshifts $z < 0.085$. This paper provides a detailed overview of the ASNOS sample selection, data reduction, SN photometry, host-galaxy spectral energy distribution construction, both global and local, and SN light-curve fitting using three methods: SALT3-NIR, SNooPy, and BayeSN. A companion paper will present the cosmological analysis.

Key words. Cosmology – supernovae – near-infrared

1. Introduction

Type Ia supernovae (SNe Ia) are thermonuclear explosions that occur in stellar systems containing at least one white dwarf (WD). The WD is supported by electron degeneracy pressure, which counteracts gravitational collapse. Several progenitor scenarios have been proposed for SNe Ia, the most common being the single-degenerate scenario (Whelan & Iben 1973), involving a WD and a main-sequence companion; the double-degenerate scenario (Webbink 1984), consisting of two WDs; as well as configurations involving triple systems (Thompson 2011), where two WDs and a tertiary star can interact to induce a direct collision between the WDs (Kushnir et al. 2013), and systems with WDs and post-AGB companions (Livio & Riess 2003; Kashi & Soker 2011). In each of these scenarios, the explosion may be triggered either by mass accretion from a companion or by stellar mergers. The explosion mechanisms include central or outer carbon ignition and surface helium ignition. These combination of

progenitor scenarios and explosion mechanisms result in either near-Chandrasekhar-mass (M_{Ch}) or sub- M_{Ch} progenitor WDs exploding as SNe Ia (Hillebrandt & Niemeyer 2000). SNe Ia can reach a luminosity around 10^{43} erg s⁻¹ at peak, and their light curves are highly homogenous, making them ideal for cosmological distance measurements. They have been used to demonstrate the accelerated expansion of the Universe (Perlmutter et al. 1999; Riess et al. 1998), as well as to measure the local expansion rate (e.g., Riess et al. 2022; Galbany et al. 2023).

In most cases, SNe Ia are observed at optical wavelengths, with more than 6,000 publicly available observed objects (Scolnic et al. 2022; Rigault et al. 2024; DES Collaboration et al. 2024). The peak *B*-band brightness of SNe Ia correlates with the post peak decline rate 15 days after maximum Δm_{15} (Pskovskii 1977; Phillips 1993) and with the *B* – *V* color at peak (Riess et al. 1996; Tripp 1998), allowing them to be used as standardizable candles after applying this correction. However, analyses of SNe Ia in the near-infrared (NIR) have shown that they are nearly natural standard candles because the NIR light is less affected by dust and they

* E-mail: phan@ice.csic.es

exhibit less intrinsic scatter in their peak luminosities (Krisciunas et al. 2004; Barone-Nugent et al. 2012; Stanishev et al. 2018; Jha et al. 2019; Müller-Bravo et al. 2022). Unfortunately, observing in the NIR is challenging due to a brighter sky background and the fact that host galaxies are often brighter than the SNe, making it challenging to accurately determine their brightness. The largest publicly available samples of SNe Ia with NIR light curves include those from the *Carnegie Supernova Project* (CSP-I: Contreras et al. 2010; Stritzinger et al. 2011; Krisciunas et al. 2017; CSP-II: Phillips et al. 2019; Hsiao et al. 2019), the Harvard Center for Astrophysics (CfA; Friedman et al. 2015), the RATIR sample (Johansson et al. 2021), SweetSpot (Weyant et al. 2018), RAISIN (Jones et al. 2022), DEHVILS (Peterson et al. 2023), and the Hawai‘i Supernova Flows (Do et al. 2024). Ongoing projects such as the Supernovae in the InFRARED Avec Hubble (SIRAH; Jha et al. in prep.; Galbany 2020) are expected to increase the sample size by a few dozen in the coming years. Currently, the total number of publicly available SNe Ia with NIR *JH*-band observations is around 300, significantly fewer than the number publicly available at optical wavelengths.

In this paper, our aim is to expand the number of SNe observed in the NIR by presenting 41 SNe with optical (*BVRI*) and NIR (*YJHK_s*) data obtained using the A Novel Dual Imaging CAMera (ANDICAM; DePoy et al. 2003) instrument mounted on the 1.3-meter SMARTS telescope at the Cerro Tololo Inter-American Observatory (CTIO). The main goal is to provide an expanded sample of SNe Ia with NIR observations in order to do precision cosmology.

Additionally, we include *JHK_s* images taken with the Son OF ISAAC (SOFI) instrument, mounted on the 3.58-meter New Technology Telescope (NTT) at La Silla Observatory. We describe the methods used to reduce the data and calculate the brightness of the SNe at various epochs to construct light curves. Then the light-curve fitting tools SNooPy (Burns et al. 2014), BayeSN (Grayling et al. 2024), and SNCosmo (Barbary et al. 2025) with the SALT3-NIR template (Pierel et al. 2022) are used to fit our data and determine light-curve parameters. Furthermore, global and local host galaxy parameters are obtained by performing photometry with Hostphot (Müller-Bravo & Galbany 2022) and conducting stellar population synthesis with Prospector (Leja et al. 2017; Johnson et al. 2021). This paper is the first of two and serves as a data reduction description and release paper, while the second paper will focus on studying Hubble diagram residuals using a combination of our data and other datasets available in the literature. The methods applied here will serve as the basis for our Aarhus-Barcelona cosmic FLOWS project, where we currently have more than 700 observations of SNe Ia in NIR.

2. Data sample

2.1. Target selection and observing strategy

Our observing campaign lasted three semesters (2018A–2019A), during which the objective was to observe approximately 12 SNe per semester. To select targets for observation, we monitored newly classified objects in the Transient Name Server (TNS¹) and ensured that each object would be observable from CTIO for about two months at magnitudes brighter than 18 mag. Although our initial goal was to select nearby objects in the Hubble flow with redshifts between $z = 0.01$ and 0.04 to accurately measure distances to their host galaxies, a few SNe at higher redshifts (but

still within the Hubble flow), were included. The objective was to obtain 10 epochs in each band (*JH*) for each SN, covering a time span from -10 to $+50$ days past the optical peak, with observations approximately every six days. This cadence would allow us to determine the peak magnitude in *JH* and capture the behavior around the secondary peak in the near-infrared. Unfortunately, the optical camera malfunctioned around April 2019, limiting our ability to obtain optical images. As a result, the last five SNe in the sample only contained *I*-band images.

2.2. ANDICAM images

The images were obtained using the SMARTS telescope at CTIO with the ANDICAM camera, which had been in operation for approximately 20 years, with its last observation taken in July 2019. We obtained simultaneous optical (*BVRI*) and NIR (*YJH*) images, with pixel scales of 0.371 and 0.271 arcsec/pixel and field-of-view (FoV) of 6×6 and 2.4×2.4 arcmin² for the optical and NIR channels, respectively. In total, 41 SNe were observed with ANDICAM, of which 29 were classified as normal SNe Ia, 8 as 1991T-like SN, 2 as 1991bg-like SN, 1 as SNe Ic-broad Line, and 1 as a 2002cx-like SN. A total of 33 out of 41 SNe had *Y*-band images, and the median number of epochs in *YJH* was 12. The optical images were taken with an exposure time of 200 sec, while the NIR images were acquired in sets of five at different dither positions by 10 or 20 arcsec, each with an exposure time of 20 sec. In the case of the *Y*-band images, only one set of dithered images was obtained, whereas two sets were taken for *JH*. A few *K*-band images were also obtained, but these were too noisy to be useful and were therefore excluded from this study. Additionally, we obtained images of standard stars on the same nights as our SN observations.

Table A.1 presents the list of SNe observed with ANDICAM, along with their sub-types, right ascensions (RA), declinations (Dec), discovery groups, classification groups, all obtained from TNS, which reports new astronomical transients such as supernova candidates. To match host galaxy and redshift, a thorough search was made in the NASA/IPAC Extragalactic Database (NED²), the SIMBAD astronomical database³, and the second data release of the Zwicky Transient Facility (ZTF DR2; Rigault et al. 2025). In the last column we also included the number of epochs in *YJH*.

2.3. Additional NIR SOFI images

Images taken with the SOFI instrument on the NTT in La Silla were obtained through the Public European Southern Observatory Spectroscopic Survey of Transient Objects (PESSTO) collaboration (Smartt et al. 2015) and typically consisted of 1 to 5 epochs of *JHK_s* images. The pixel scale is 0.25 arcsec/pixel, and the images cover a FoV of 5×5 arcmin². A summary of images collected with SOFI is also included in Table A.1.

2.4. Additional optical data

In addition to our optical ANDICAM images, we also obtained optical data from the Asteroid Terrestrial-impact Last Alert System (ATLAS; Tonry et al. 2018) and the Zwicky Transient Facility (ZTF; Bellm et al. 2018). ATLAS is a highly efficient system for detecting potentially hazardous asteroids, as well as tracking and discovering transients, with a two-day cadence in the cyan

¹ <https://www.wis-tns.org>

² <https://ned.ipac.caltech.edu/>

³ <https://simbad.cds.unistra.fr/simbad/>

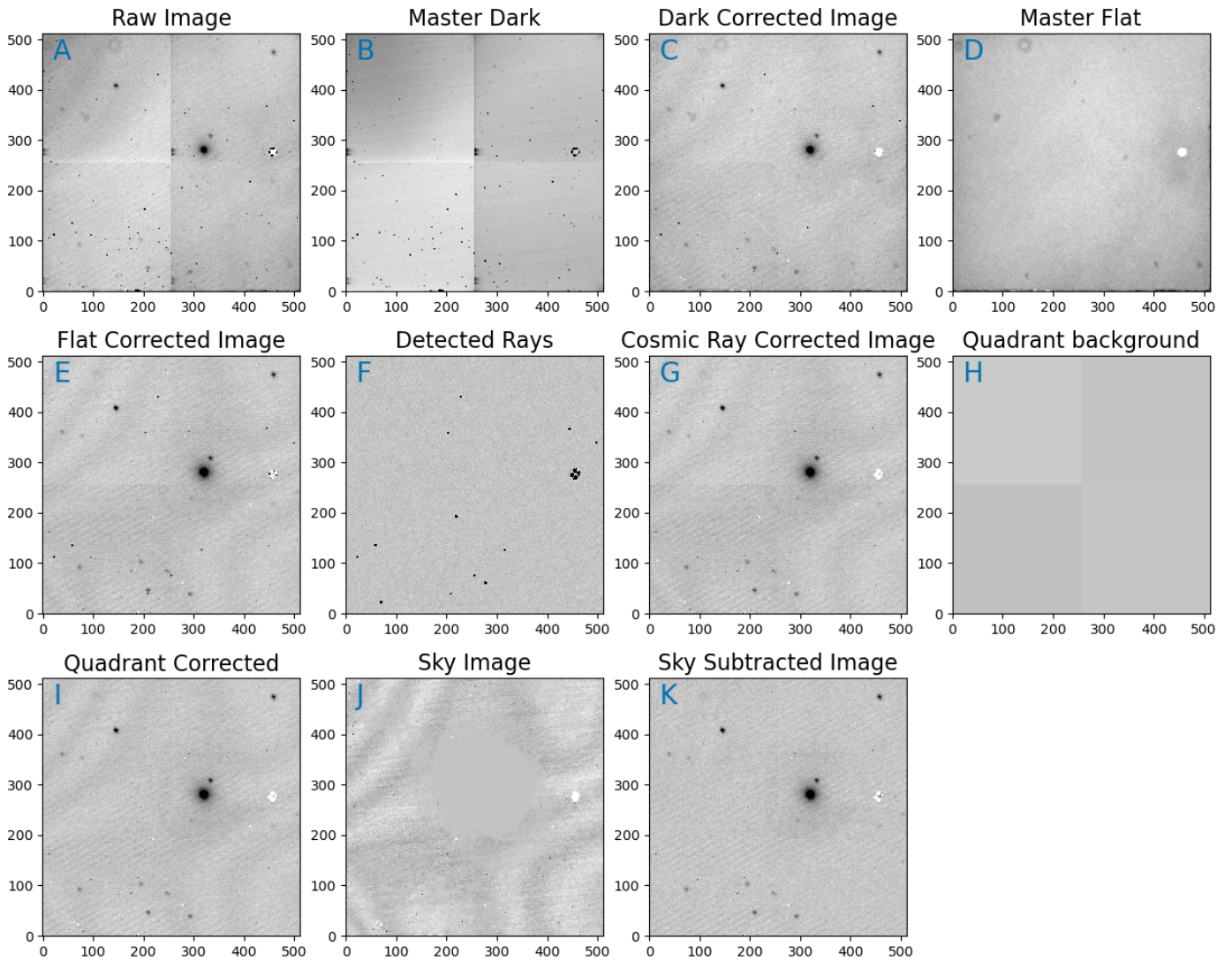


Fig. 1: Example of raw image reduction for ANDICAM *J*-band image. Top row (left to right): Single raw image of SN 2019so, master dark, dark reduced raw image using the two previous images and master flat. Middle row: Flat and dark reduced image, detected cosmic rays, cosmic ray corrected image and quadrant background level. Bottom row: Image corrected for quadrant features, sky image, and sky subtracted image. The sky image was evaluated from the remaining set of dithered images taken on the same night. The host galaxy was masked out for each single image when constructing the sky image.

band (*c*; 4200–6500 Å) and orange band (*o*; 5600–8200 Å). Currently, ATLAS observes the whole sky with a cadence of one day between declinations of -50 and $+50$ and two days in the polar regions, weather permitting. The images were calibrated using the Pan-STARRS catalog (Chambers et al. 2019), and the light curves are publicly available through The Atlas Project Fallingstar photometry service.⁴ Optical data from ZTF were retrieved from the ZTF second data release (Rigault et al. 2025) and was obtained using the Palomar 48-inch Schmidt telescope, which scanned the entire northern sky visible from Palomar every two days in the *g*- (3676–5614 Å) and *r*-band (5498–7394 Å), while alerts will be distributed in real time to the brokers for the *i*-band (6870–8964 Å).

2.5. Host-galaxy template images

In cases where the SN occurred in a bright region of the galaxy, it was crucial to remove the underlying host-galaxy light contamination to precisely measure the SN brightness in the image. This was done by checking that the background level around the SN was close to 0. Ideally, host-galaxy template images should be taken with the same instrument; however, ANDICAM stopped operating right after our program ended in July 2019. As a result, we had to either rely on archival images or obtain new images with other facilities.

The NIR images were obtained through the European Southern Observatory (ESO) archive⁵ and The United Kingdom Infrared Telescope (UKIRT) Hemisphere Survey archive.⁶ We also attempted to use 2MASS templates, but the resolution of these images was insufficient to provide a good subtraction. If

⁴ <https://atlas.fallingstar.com>

⁵ <http://archive.eso.org/scienceportal/home>

⁶ <http://wsa.roe.ac.uk/index.html>

no archival templates were available, new templates were obtained using the NOTCam camera at the 2.5-meter Nordic Optical Telescope (NOT) in La Palma or SOFI at the NTT in La Silla through the PESSTO collaboration. Furthermore, our project was awarded one night to observe at the 6.5-meter Magellan Baade telescope using the FourStar instrument (Persson et al. 2013) located on Las Campanas Observatory in Chile. Optical template images on the other hand were obtained from the Dark Energy Survey⁷ (DES), Pan-STARRS⁸, SkyMapper⁹, or EFOOSC at NTT (again through the PESSTO collaboration). In a few cases, when it was not possible to obtain *BVRi* templates for subtraction, we used *g*-band templates for *B* and *V*, *r* for *R*, and *i* instead of *I*. Since all NIR template images were taken in 2023 or later, the SNe had long since faded, as our SNe were observed in 2018–2019.

3. Data reduction

3.1. Optical ANDICAM imaging

The optical ANDICAM images were directly retrieved from the SMARTS FTP archive and had already been reduced using the dedicated ANDICAM pipeline¹⁰, which applies bias and flat-field corrections to the images.

3.2. NIR ANDICAM imaging

NIR images were provided in raw format, so we describe the data reduction process here, including flat-field and dark corrections, sky subtraction, and the combination of dithered images.

3.2.1. Flat and dark correction

To reduce our ANDICAM NIR images as well as our standard stars, we used CCDPROC¹¹, an Astropy-affiliated package for the reduction of charge-coupled device (CCD) images. This allowed us to take an image in FITS format and convert it into a CCD-DATA object, which is a matrix containing the photon counts at each pixel position in our images. Flats were already combined into master flats and made available in the SMARTS FTP archive. Individual dark frames taken during a night were combined into a master dark. To create the master dark for a given date, all dark images taken on that date were collected and CCDPROC.COMBINE was used to combine the dark frames entrywise by taking the median. Because flats and darks were not taken every night, we selected the flat and dark images from the FTP archive that were closest in time to when the raw science images were taken (typically 2–3 days apart at worst). Both the master flat and master dark were used for the SN images and standard stars. The master dark was subtracted from each raw image using CCDPROC.SUBTRACT_DARK, which scales the master dark to match the exposure time of the raw image and then subtracts it. In our case, the exposure times were the same, so no scaling was needed. Finally CCDPROC.FLAT_CORRECT was used to normalize the master flat using the median of the matrix (if not already done) and then divided the dark-subtracted images by the flat entrywise.

Figure 1 illustrates the process of dark and flat correction for a single raw image. We note the presence of an artifact in the middle-right of all our images, which could not be entirely removed during the master flat correction. However, this artifact does not affect the SN magnitude, as the SN is consistently positioned near the center in all our images. For the *Y*-band images, no *Y*-band flats were available in the SMARTS FTP archive, so a *J*-band flat was used instead. By comparing the differences between the *J*- and *H*-band flats, it was found that the variation between them is less than 2%, resulting in differences in instrumental magnitudes of local sequence stars of 0.02 magnitudes in the worst cases (going in both directions). As a result, an uncertainty to the instrumental magnitude in the *Y*-band of 0.02 magnitudes was added in quadrature. Because the *Y*-band photometry may have an $\sim 2\%$ offset arising from the use of *J*-band flats during data reduction, we do not recommend using these data for precision cosmology and exclude them from our light-curve fitting.

3.2.2. Cosmic ray removal

Cosmic rays were removed using the COSMICRAY_LACOSMIC module from CCDPROC, which detects and removes cosmic rays based on the readout noise, a sigma detection threshold (which was set to the default value of 5), and the science image as input parameters. Image F in Figure 1 shows the detected cosmic rays, and the image corrected for cosmic rays is seen in image G.

3.2.3. Quadrant Correction

In some science images, the background levels differ between quadrants, which can be seen in image G in Figure 1. To address this issue, the image was divided into four quadrants, and bright sources were masked out. The background level in each quadrant was then estimated and subtracted accordingly. The estimated background level for each quadrant can be seen in image H of Figure 1, while the science image corrected for quadrant features can be seen in image I. Before subtracting the quadrant backgrounds, the overall background level of the full image was estimated and stored for later use in rescaling the final science frame. Additionally, the background level was used to select images with the similar background levels to construct a sky background (see Sect. 3.2.4 for more details).

3.2.4. Sky subtraction

The next step was to remove the sky background, which can vary significantly in the NIR, even when images were taken just a few minutes apart. To achieve this, the following procedure for a set of dithered images was used: At a given epoch, the median and standard deviation of all images were evaluated. These values were saved to rescale the final science image afterwards, ensuring that reliable uncertainties for photometry were maintained. We estimated the standard deviation of the sky medians and named this value “*sky_std*”. Similarly, we estimated the average of the standard deviations and named this value “*sky_noise*”. If *sky_std* < *sky_avg*, some images had background levels that were different from the rest. These were excluded until *sky_std* > *sky_avg*. Then, for a given image in a set of dithered images, CCDPROC.COMBINE was used on the remaining images to create a sky background. Finally, the sky background was subtracted from each image. In some cases, a large object such as the host galaxy could be bigger than the

⁷ <https://www.darkenergysurvey.org>

⁸ <https://outerspace.stsci.edu/display/PANSTARRS/>

⁹ <https://skymapper.anu.edu.au>

¹⁰ <http://www.astro.yale.edu/smarts/ANDICAM/data.html>

¹¹ <https://github.com/astropy/ccdproc>

dithering step size, which could result in a brighter sky image around the location of the host galaxy. To address this issue, bright sources were masked out in each image before combining into a single sky image.

Image J of Figure 1 shows the sky image with the area around the host galaxy masked out, and the final sky-subtracted image is seen in image K. Here, it was possible to successfully capture and remove the wave-like structure present in the sky background from the dark- and flat-corrected image.

3.2.5. World Coordinate System

Only the NIR ANDICAM images did not have any World Coordinate System (WCS) values in the image header so to obtain these, we used `nova.Astrometry.net`¹², which requires at least three stars that can be detected by the code. This turned out to be difficult, as the stars were faint and the FoV was quite small (2.4×2.4 arcmin²). For SN 2018hhn, SN 2018jag and SN 2019cxx, it was not possible to obtain a WCS. Therefore these images were combined using the relative position of the host galaxy. This turned out to be successful for SN 2018hhn and SN 2018jag, while it was not possible to detect any stars/galaxies in the images of SN 2019cxx.

3.2.6. Combined final images

The dithered images can now be combined into a single science image. To do this, each image was projected onto a grid of NaNs based on the relative position of a star. From the list of grids, we used `NUMPY.NANMEDIAN` to combine the images. Finally, the edges were cropped to ensure the final image had at least 50 percent of the coadded images throughout.

3.3. Complementary imaging

As aforementioned, we also obtained data from SOFI, ZTF, and ATLAS, which are used in the SN Ia template light-curve fitting process. ZTF light-curves were retrieved from ZTF DR2 (Rigault et al. 2024). Below, the data reduction processes for each of the other datasets are described in detail.

3.3.1. SOFI

The raw SOFI NIR sciences images, flats, and darks were downloaded from the ESO archive¹³ and reduced using the PESSTO pipeline.¹⁴ This pipeline handles the flat and dark corrections of the raw science images, as well as the sky subtraction and individual frame combination.

3.3.2. ATLAS

The ATLAS data were obtained through the ATLAS forced photometry homepage. We requested epochs between -50 to $+100$ days of the detection date of the SN to make sure the LC peak(s) were obtained. ATLAS often took four measurements per night so the data was stacked following The Atlas Project's Python plotting software (Young 2020). The fluxes and errors in the output file were given in microJansky, denoted μJy and $d\mu Jy$, respec-

tively. The fluxes were converted into AB magnitudes using

$$m_{AB} = -2.5 \cdot \log_{10}(\mu Jy) + 23.9. \quad (1)$$

For the magnitude error, the homepage suggested to do a Taylor expansion of $\log_{10}(\mu Jy + /-d\mu Jy)$ when $d\mu Jy/\mu Jy$ was small, but since this was not always the case, we chose to do error propagation instead, where we set

$$m_{AB, err} = \frac{2.5}{\ln(10)} \cdot \frac{d\mu Jy}{\mu Jy}. \quad (2)$$

Non-detections were removed using a 3σ upper limit

$$m_{3\sigma} = -2.5 \cdot \log_{10}(3 \cdot d\mu Jy) + 23.9. \quad (3)$$

In general, baseline correction were not required for ATLAS photometry. However, there are two epochs in which ATLAS changed reference images and therefore the baselines changed. In the cases of SN 2018bie and SN 2018exc, we observed that non-detections both before and after the SN light curve exhibited flux values significantly deviating from zero (≈ -600 in flux space). Notably, around 400 days post-explosion, these non-detections returned to zero flux. Without applying a baseline correction, the apparent magnitudes appeared artificially faint. To account for this, a baseline correction was implemented exclusively for these two SNe. The baseline level was determined using a trimmed mean of flux values from epochs earlier than -30 days and later than $+400$ days relative to the SN detection date, ensuring that any residual supernova signal was excluded. When performing light-curve fitting (see Sect. 5), the resulting fits were significantly improved with the baseline correction, whereas the fits were poor when no correction was applied.

3.4. Background subtraction

Lastly, the background was subtracted from the optical ANDICAM images as well as SOFI images (this was already done for the NIR ANDICAM images). The background was subtracted using `BACKGROUND2D` from `PHOTUTILS.BACKGROUND`. Here `MEDIANBACKGROUND` was used, which calculated the background in an array as the sigma-clipped median, with sigma set to 3. Figure 2 shows an example of background subtraction. All reduced images can be accessed from GitHub.¹⁵

4. Photometry

Here, we describe the methods used to determine the apparent magnitudes of our SNe and construct light curves. This process includes template subtraction, aperture photometry, calculating zeropoints, and determining color term coefficients. Color term coefficients quantify how a natural system differs from the standard system as a function of the color of an object and allows one to transform magnitudes from one system to the other. A natural system refers to the photometric system native to the telescope and detector setup, or in other words the system response function, while a standard system refers to a widely used photometric system such as the Johnson system. Here the objective is to construct SN light curves in the natural system.

¹² <https://nova.astrometry.net>

¹³ http://archive.eso.org/eso/eso_archive_main.html

¹⁴ <https://github.com/svalenti/pessto>

¹⁵ <http://www.github.com/SN-ICE/ASNOS>

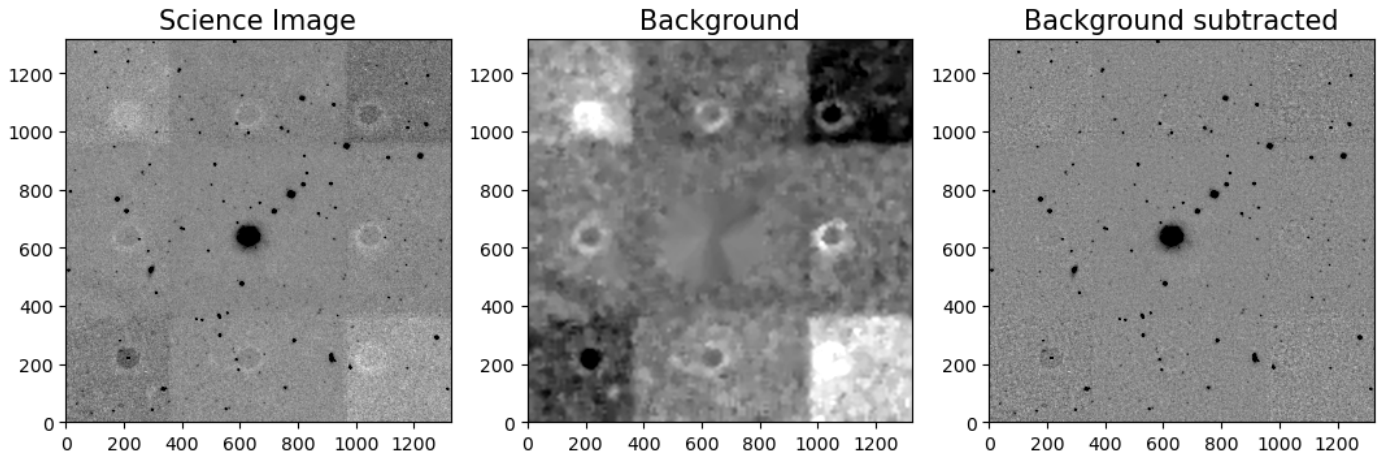


Fig. 2: Example of background subtraction for a SOFI image. *Left*: Combined J -band science image of SN 2018agk taken with SOFI. *Middle*: Detected image background using `PHOTUTILS.BACKGROUND2D`. *Right*: Background and cosmic ray subtracted image. It is seen that we were able to remove most quadrant structure of the image.

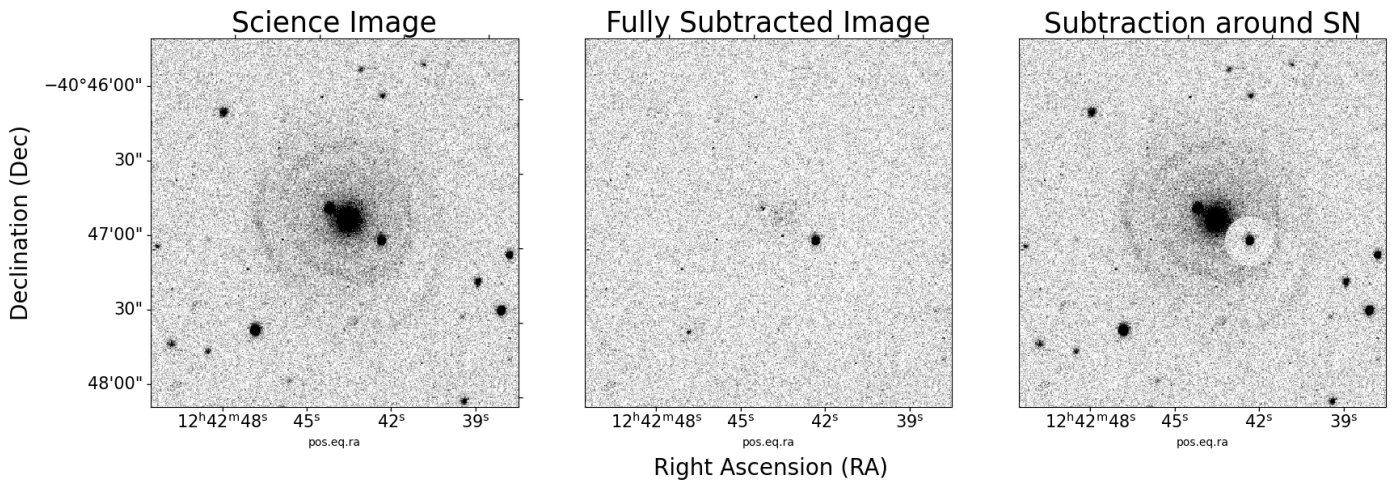


Fig. 3: Template subtraction using `ImageMatch`. *Left*: Science image without template subtraction. *Middle*: Fully subtracted science image. *Right*: Template subtracted image using `ImageMatch` with the SN in the middle of the subtracted area. `ImageMatch` does subtraction on the full image, but one can choose to have the subtracted area around the SN inserted back into the original science image, which allowed us to use local sequence stars to determine zeropoints.

4.1. Template subtraction

Before our images could be used for photometry, the light from the host galaxy was removed using the software `ImageMatch`.¹⁶ This software rectifies an image by matching point-sources from the science image to the host-galaxy template and solving for a geometric transformation from one to the other. Afterwards it convolved one image with a “seeing kernel” that blurred it so that they matched in resolution, which resulted clean subtractions. Only in a few cases, the seeing in the science image was better than the template, and therefore the science image needed to be blurred so it matched the template in order to do proper subtraction. By default, `ImageMatch` performs subtraction over the entire image. For photometric measurements, a small region centered on the SN from the subtracted image was instead inserted into the original, unsubtracted frame containing all field stars. This procedure allowed the SN’s apparent magnitude to be estimated in a single step: first determining the zeropoint from

local sequence stars and then measuring the SN’s instrumental magnitude. To assess the quality of the subtraction, the entire subtracted image was visually inspected to confirm that nearby stars and galaxies were properly removed.

Figure 3 shows an image before and after subtraction. It is clearly seen that the light from the host galaxy had been subtracted around the SN. For a few cases, it was not possible to do proper subtraction when the SN was at the center of the host. This was likely due to the fact that templates and science images were from other instruments/filters. This happened to SNe 2018dda, 2018exb, 2018exc, and 2018feq. Light curve fitting were attempted for these SNe, but since the fits were bad and the SN was not clearly isolated, these images were not used.

To check the effect of our template subtractions, a comparison between the apparent magnitude of various SNe with and without subtraction was made based on how far away from the host they were. This was accomplished using the angular distance to the SN normalized by the host galaxy’s directional light radius denoted d_{DLR} (Sullivan et al. 2006; Gupta et al. 2016; Sako et al. 2018) and depends on the shape of the galaxy and

¹⁶ <https://github.com/obscode/imagematch>

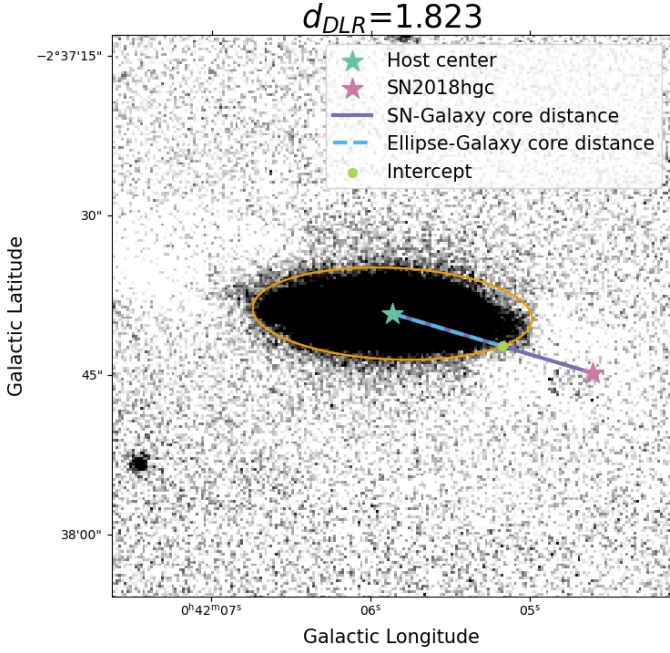


Fig. 4: Example of measuring d_{DLR} . The shape of the host was measured using *sep* and plotted in orange. The d_{DLR} is the ratio between distance from the host center to the SN (purple) and the distance from the host center to the edge of the ellipse (dashed blue).

the SN direction. Generally $d_{DLR} < 1$ means that the SN is inside the ellipse of the host galaxy, while $d_{DLR} > 1$ means it is outside and therefore would be minimally affected much by the light of its host. Hence SNe with $d_{DLR} > 1$ could be used as a consistency check to see if our subtractions were impactful or not. The software *SEP*¹⁷ was used to determine the shape of the host galaxy. *SEP* is a python implementation of *SOURCE EXTRACTOR*¹⁸ and determines the sizes and shapes of stars/galaxies in an image in terms of elliptical parameters such as semimajor and semiminor axis. Figure 4 shows an example of how d_{DLR} was evaluated for a host galaxy with its shape (in orange) determined from *SEP* using a 3-sigma detection threshold. Table A.1 shows d_{DLR} for all SN hosts in our sample. In each case, *r*-band images were used (mostly from Pan-STARRS, SDSS, DES). The results of estimating d_{DLR} for a few SNe are shown in Figure 5. The top panels show the apparent magnitude of some SNe with different d_{DLR} with subtraction (filled circles) versus no subtraction (empty circles) for the ANDICAM *BVRI*. The bottom panels show the corresponding histograms of the apparent magnitude difference between non-subtracted and template subtracted images, where the median difference is presented in the legend. Not surprisingly, there was not much difference between subtracted and non-subtracted images when the SN was far away from its host, while there was significant contamination from the host when the SN was close.

4.2. Absolute Photometry

To evaluate the brightness of the local sequence stars and the SN in our images, the *PHOTUTILS*¹⁹ package was used. With

DAOSTARFinder, sources in our images that were 3σ above background level were detected. Each source was then fitted with 2D gaussian to determine their geometric properties such as position, semimajor axis, semiminor axis and full-width-at-half maximum (FWHM), which is the width of the distribution measured between two points where the value of the curve is at half its maximum amplitude. The world coordinate system (WCS) in the image header was used to assign catalog magnitudes to each object if the relative distance between the position obtained from DAOSTARFinder and the catalog position was less than 0.5 FWHM.

4.2.1. Reference Catalog

The ATLAS-REFCAT2 catalog (Tonry et al. 2018), an all-sky reference catalog containing about one billion stars down to an apparent magnitude of 19, was used to assign catalog magnitudes to our sources. REFCAT2 consists of a variety of surveys such as PanSTARRS, The AAVSO Photometric All-Sky Survey (APASS), SkyMapper and the Two Micron All Sky Survey (2MASS). The PanSTARRS magnitudes (*gri*) from ATLAS-REFCAT2 were transformed into Johnson *BVRI*, which corresponded to the optical passbands of ANDICAM, using the transformations in Tonry et al. (2012)

$$\begin{aligned} B_{cat,std} &= g_p + 0.213 + 0.587 \cdot (g_p - r_p) \pm 0.034, \\ V_{cat,std} &= r_p + 0.006 + 0.474 \cdot (g_p - r_p) \pm 0.012, \\ R_{cat,std} &= r_p - 0.138 - 0.131 \cdot (g_p - r_p) \pm 0.015, \\ I_{cat,std} &= i_p - 0.367 - 0.149 \cdot (g_p - r_p) \pm 0.016, \end{aligned} \quad (4)$$

where the “*p*” subscript denotes Pan-STARRS passbands, and the “cat,std” subscript denotes the catalog magnitude in a standard photometric system such as the Johnson system. The ANDICAM *Y* passband was similar to the Dark Energy Camera (DECam) *Y* passband so our catalog magnitudes had to be transformed into DECam magnitudes. As color term coefficients would be determined later on, we evaluated DECam *z*-band magnitudes as well in order to have a filter that was close to the *Y* band in terms of wavelength range. This required Pan-STARRS *zy* bands, but since the ATLAS-REFCAT2 only had PanSTARRS *griz*, we used the 2MASS transformations from Tonry et al. (2012) to obtain the PanSTARRS *y* band

$$y_p = J_2 + 0.531 + 0.916 \cdot (J_2 - H_2) \pm 0.061, \quad (5)$$

where the 2 subscript denotes 2MASS magnitudes. Finally the transformations from Abbott et al. (2021) were used to obtain DECam *zY* magnitudes

$$\begin{aligned} z_{DES} &= y_p - 0.031 \cdot (r_p - i_p) - 0.01 \pm 0.015, \\ Y_{DES} &= y_p - 0.031 \cdot (r_p - i_p) + 0.035 \pm 0.017. \end{aligned} \quad (6)$$

Before we determined the instrumental magnitude of our sources, a few cuts were applied: 1) Objects that were $3 \cdot FWHM$ from the edges of our images were removed (our images consisted of multiple dithered images, and therefore stars closer to edge had less images compared to the center, which therefore gave less precise measurements). 2) Galaxies were removed. 3) Saturated objectives were removed. This was achieved by calculating the maximum pixel value for each source and remove objects where the detector limit was exceeded and the detectors would go non-linear. For ANDICAM optical, ANDICAM NIR and SOFI, the limits were 45000, 5000 and 10000 ADU, respectively.

¹⁷ <https://sep.readthedocs.io>

¹⁸ <https://www.astromatic.net/software/sextractor/>

¹⁹ <https://photutils.readthedocs.io/en/stable/index.html>

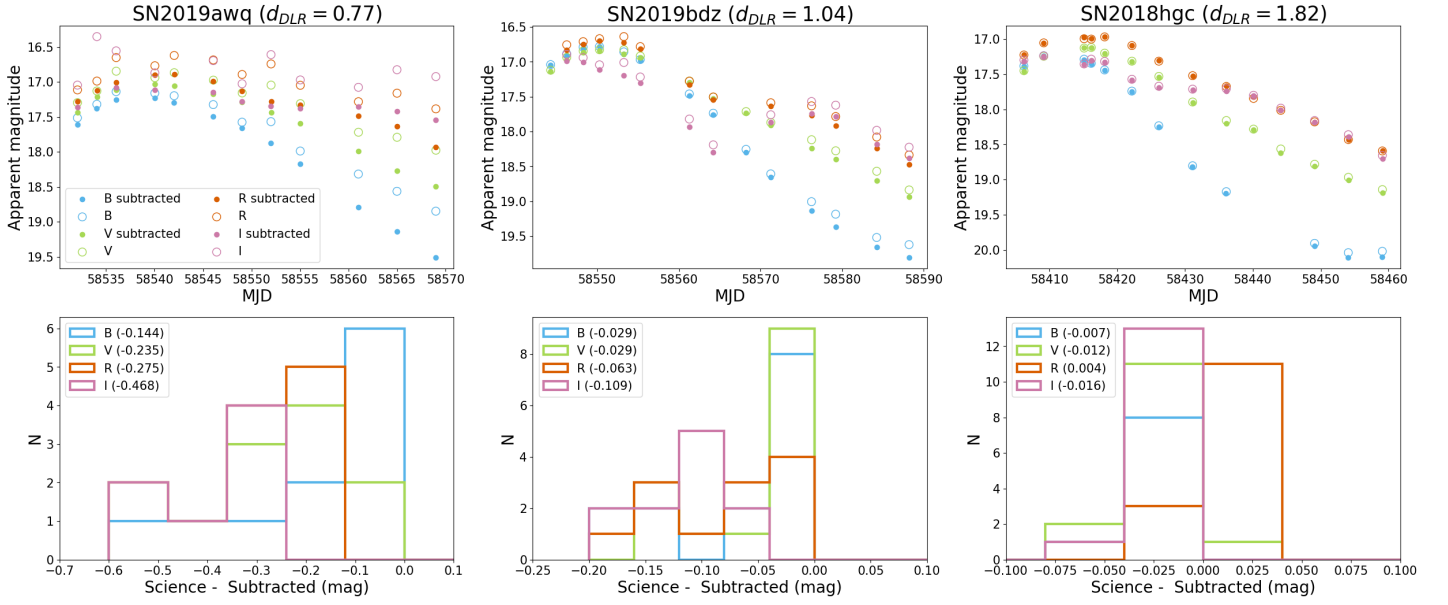


Fig. 5: *Top panels:* Comparison of photometry using subtracted images (filled circles) vs. not using templates (empty circles) for SNe with different d_{DLR} . As expected, applying host-galaxy template subtraction to the science images did not have a huge effect on the light curve when the SN was far from its host ($d_{DLR} > 1$). On the other hand, the effect was significant when $d_{DLR} < 1$, showing why template subtractions were important. *Bottom:* Histogram of the apparent magnitude difference between subtracted and non-subtracted images. The median value is reported in the legend for each filter.

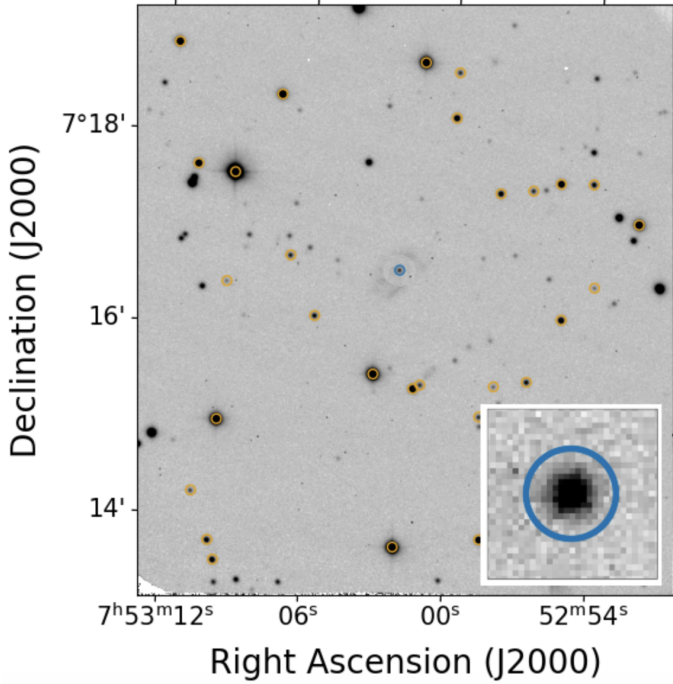


Fig. 6: Aperture radii (orange for local sequence and blue for supernova) for one of our science images. To determine the aperture radius (the same aperture is used for all sources), we fitted a 2D gaussian to all local sequence stars and evaluated a 3σ -clipped median of the FWHM, and multiplied this by 0.6734 to obtain the aperture radius. The inset at the bottom right is a zoom-in of the SN and its aperture.

4.2.2. Instrumental Magnitude

To determine the natural instrumental magnitudes of our sources, we used `CIRCULAR_APERTURE` from `PHOTUTILS.APERTURE`, which evaluated the total counts within a circle of a given radius. For each image, a 3σ -clipped median of the distribution of FWHM of our local sequence stars was evaluated. The aperture radius of all our sources (including the SN) was then set to be 0.6731 times the median FWHM, which is the optimum aperture size for photometry of sources whose profiles can be approximated as Gaussian.²⁰ An example of this procedure can be seen in Figure 6.

To convert the counts inside the apertures into instrumental magnitudes in the natural system $m_{inst,nat}$ (i.e., the magnitude system measured by the telescope), we used

$$m_{inst,nat} = -2.5 \cdot \log_{10}(Counts/t_{exposure}), \quad (7)$$

where $t_{exposure}$ is the total exposure time divided by the number of coadds (for ANDICAM NIR this is just the exposure time of a single image since the coadded images are divided by the mask). To correct for extinction, say for the *B*-band, we used the equation

$$B_{inst,cor} = B_{inst,nat} - k_B \cdot X. \quad (8)$$

Here k_B is the extinction coefficient, X is the airmass value and was taken from the image header, and $B_{inst,nat}$ is the natural instrumental magnitude from Eq. 7. Table 1 in Stritzinger et al. (2005) was used to correct for extinction the ANDICAM *BVR/IR* passbands from the central wavelength of each filter. The estimated extinction coefficients are shown in Table 1. In their work, they evaluated extinction coefficients at CTIO out to 11000 Å, and the value at this wavelength was 0.003. Because this value is small, extinction corrections to the ANDICAM *JH* filters were

²⁰ <https://wise2.ipac.caltech.edu/staff/fmasci/GaussApRadius.pdf>

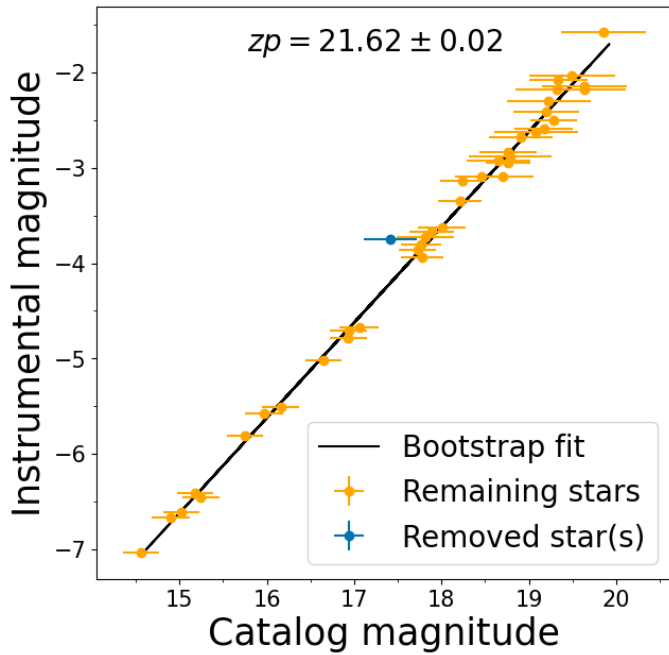


Fig. 7: Example of calculating an image zeropoint using bootstrapping with sigma clipping as outlier rejection, where the standard deviation from Chauvenet’s criteria was used. At the top of the panel we show the image zeropoint and its error, the black line is the fit using a linear function in the form of $f(x) = x + b$, and the orange points are the stars that remain after doing sigma clipping, and the blue point(s) are rejected stars. The zeropoint is the intercept value from the fit.

not applied. Likewise, when we looked at the La Silla Observatory’s homepage,²¹ there are only extinction coefficients out to 9000 Å, and the value at this wavelength was 0.01. Therefore, the extinction coefficients in JHK_s were assumed to be zero.

4.3. Image Zeropoints

The method used to evaluate the zeropoint for the science images is described here.

4.3.1. ANDICAM optical and SOFI

After making cuts described in the previous section, We determined the zeropoint from sigma clipping using Chauvenet’s criterion. A linear function with a slope of unity in the form of $f(x) = x + b$ was fitted, where the zeropoint is the intercept in the instrumental versus catalog magnitude plot, where for a given star the instrumental magnitude is given by Eq. 8. Figure 7 shows an example of evaluating the image zeropoint, where sigma clipping was used to remove outliers. The error was set to be the weighted mean of the residuals between the fit and the data. Notice that the zeropoints estimated here were not the final zeropoint; they would only be used to determine color term coefficients through an iterative process.

More generally, the y-axis in Figure 7 is the B -band instrumental magnitude in the ANDICAM natural system $B_{inst,nat}$, while the x-axis is $B_{cat,std} - CT_B \cdot (B - V)_{cat,std}$, where the “cat,std” subscript denotes a catalog magnitude in the Johnson

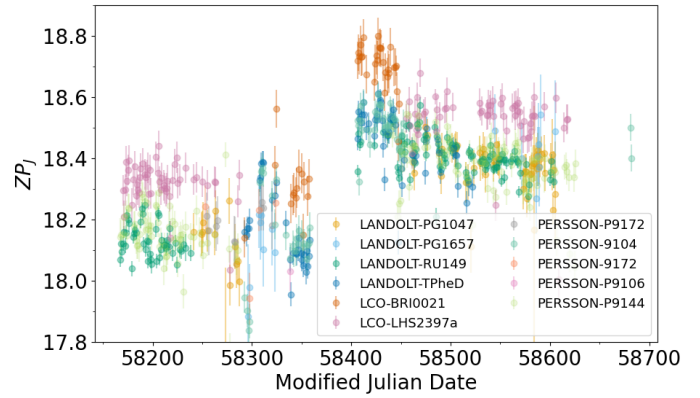


Fig. 8: J -band zeropoints for different nights. The zeropoints were computed using $J_{inst} - J_2$, where J_{inst} is the instrumental magnitude evaluated from aperture photometry and J_2 is the 2MASS catalog magnitude in the J band. It is seen that standards taken at the same night give different zeropoints, making the standards too uncertain.

standard system, and CT_B is the B -band color term. Initially, the color term was unknown so the x-axis in this case was $B_{cat,std}$. The idea was to use the initial image zeropoint point to estimate an initial color term. With the initial color term, a new image zeropoint could be estimated from the $B_{cat,std} - CT_B \cdot (B - V)_{cat,std}$ versus $B_{inst,nat}$ plot, which in turn would yield a new color term and so forth. This iterative process will be described in greater detail in Sect. 4.4.

4.3.2. ANDICAM NIR

We evaluated the zeropoints of our standard field observations by plotting them as function of observation date, as shown for the J band in Fig. 8. Even though standards were observed at the same nights, the zeropoints could differ by half a magnitude, which should not be the case. This issue was also seen in Wang et al. (2020), who found differences in the nightly zeropoints of NIR standards using ANDICAM, and therefore they used field stars that had magnitudes in the 2MASS catalog. Attempts to apply color-term coefficients did not significantly improve the calibration. Consequently, these standard star fields were not used; instead, local sequence stars with catalog magnitudes from REFCAT2 were adopted to determine the image zeropoint.

4.4. Color term coefficients

Ideally, color-term coefficients should be determined for each field-of-view on a given night, but the limited number of local sequence stars in most images makes this unfeasible. Instead, stars observed across all epochs were combined. To determine the color-term coefficients, for example, for the B band, the quantity $B_{cat,std} - B_{inst,cor} - ZP_{B,img}$ was plotted against $(B - V)_{cat,std}$ for all B -band images, and the slope of the relation was determined. Here $ZP_{B,img}$ is the image zeropoint, which was determined following the procedure in Sect. 4.3.1.

For a given star observed at various epochs, a 3-sigma clipping was made to remove outliers, and if the residuals were greater than 0.5 mag for a given star, it was rejected. By doing this, potential variable stars were also excluded. Additionally, we only selected stars whose uncertainties in

²¹ <https://www.eso.org/sci/observing/tools/Extinction.html>

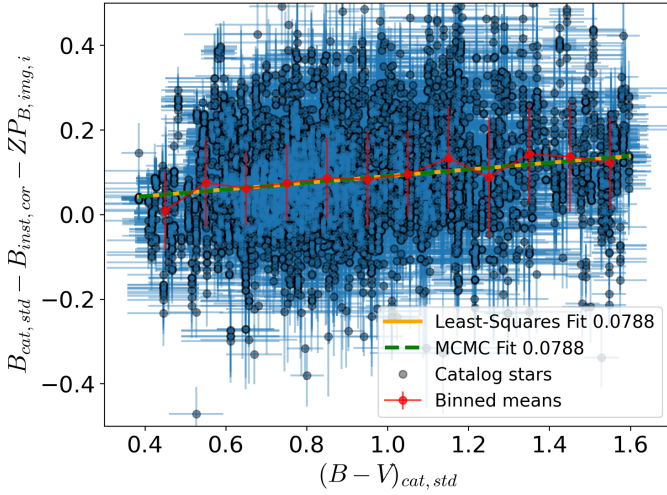


Fig. 9: Sigma-clipped $B_{cat,std} - B_{inst,cor} - ZP_{B,img,i}$ vs. $(B - V)_{cat,std}$ for all B band images in the sample (black). We estimated binned means (red) and their uncertainties and removed very red/blue stars if the bins did not agree with the fit. The legend gives the slope using Scipy least squares (orange) and the MCMC fitting code Emcee (green), which shows that the values agree.

instrumental magnitudes were less than 0.05 mag. The slope of the $B_{cat,std} - B_{inst,cor} - ZP_{B,img}$ versus $(B - V)_{cat}$ plot was determined using Markov Chain Monte Carlo (MCMC) with the Emcee package²².

The fitted slope to this data only provided an approximate color term coefficient, as the $ZP_{B,img}$ obtained in the previous step, which was used to ensemble the data from all night into the same scale, did not include any color term correction. Therefore, an iterative approach was taken, where we recomputed the zero-point using the catalog magnitudes corrected by the newly computed color-terms. Subsequently, the new zero point value $ZP_{B,img,i}$ was used in the process of obtaining a new color-term coefficient $CT_{B,i}$. This process was iterated until the color-term value converged to four significant digits. This iterative process was essential because the zero-point and color-term coefficient were interdependent and could only be solved by cyclic computation of the coefficients. More specifically, $CT_{B,i}$ was used to color correct the catalog magnitude as $B_{cat,std} - CT_{B,i} \cdot (B - V)_{cat,std}$, and a new image zeropoint, $ZP_{B,img,i}$, was then evaluated in the same manner as in Fig. 7 from the $B_{inst,nat}$ versus $B_{cat,std} - CT_{B,i} \cdot (B - V)_{cat,std}$ plot. All B -band images were then used to determine a new slope from the $B_{cat,std} - B_{inst,cor} - ZP_{B,img,i}$ versus $(B - V)_{cat,std}$ plot. The iterations continued until the slope value converged to four significant figures, which typically occurred after five iterations. Figure 9 shows the results of the Emcee fit for the final iteration (green) along with the slope determined from a least squares fit in Scipy²³ (orange), where it is seen that the Scipy and Emcee results agree. The mean and standard deviation were estimated for multiple color bins, and stars with extreme colors were excluded if the binned mean value was a 1σ outlier from the fitted relation.

Table 1 shows the estimated color term coefficients for ANDICAM and SOFI, and Fig. F.1 in the Appendix shows the corresponding fit for each filter. We noticed that the color term

coefficient for Y was quite large, which was likely due to a small number of local sequence stars and narrow color range. For K_s the color term was large, but the error was only around 5%, which suggested that the SOFI K_s filter was different from the 2MASS K_s . After the color term coefficients were evaluated, it was now possible to evaluate the SN magnitude in the natural system. Firstly, the catalog magnitudes of the local sequence stars in the standard system were transformed into the natural system. The relation between natural and standard magnitudes for the B band is

$$B_{cat,nat} = B_{cat,std} - CT_B \cdot (B - V)_{cat,std}, \quad (9)$$

where CT_B is the B -band color term coefficient. The newly obtained natural catalog magnitudes were then used to evaluate the natural image zeropoint $ZP_{img,nat}$ using the same procedure described in Sect. 4.3.1, with the only difference being that the catalog magnitude has been transformed to the ANDICAM natural system, and the instrumental magnitudes are in the natural system and not corrected for extinction. With the natural image zeropoint, the apparent magnitude of the SN in the natural system is obtained following

$$m_{B,SN,nat} = B_{SN,inst,nat} + ZP_{img,nat}, \quad (10)$$

where $m_{SN,nat}$ is the instrumental magnitude of the SN. Notice that no extinction correction are applied to the local sequence stars/SN, as they were observed in the same small FoV and therefore experience the same amount of airmass and extinction.

5. Light curve fitting

We here describe the light curve fitting techniques SALT3-NIR, SNooPy and BayeSN that were used to fit our light curves. For all three cases a flat Λ CDM universe with $\Omega_{m0} = 0.3$ and $H_0 = 70 \text{ km s}^{-1} \text{ Mpc}^{-1}$ was used. Furthermore, the dust maps from Schlegel et al. (1998) was used to obtain the Milky Way color excess and, the reddening laws from (Cardelli et al. 1989) are used to determine Milky Way extinction for SNooPy and SALT3 and (Fitzpatrick 1999) for BayeSN (Cardelli would have been used for BayeSN if it were possible, but this was not the case).

5.1. SALT3-NIR

SNCosmo²⁴ is a Python library for supernova cosmology analysis. To perform light curve fitting in SNCosmo, we used the SALT3-NIR model (Pierel et al. 2022), which is an extension of the SALT3 model (Kenworthy et al. 2021). This allowed us to do light-curve fitting in the NIR and had been trained on around ~ 1000 SN Ia with data at optical wavelengths, and as well as 166 objects with NIR light curves. Additionally, SALT3-NIR was also trained with optical and NIR spectra to perform K-corrections. Output parameters include amplitude x_0 , which is related to the B -band peak magnitude ($B_{max} \sim -2.5 \cdot \log_{10}(x_0)$), time of maximum t_0 , stretch x_1 , which is related the shape of the LC, and color c , which describes the supernova color (due to dust extinction or intrinsic properties). However, the model only goes out to 20000 \AA and therefore K_s -band images from SOFI could not be included.

For optical wavelengths, there were issues combining ATLAS data with our optical ANDICAM data; in some cases, fitting ATLAS only or ANDICAM only provided successful fits,

²² <https://emcee.readthedocs.io/en/stable/>

²³ <https://docs.scipy.org/doc/scipy/>

²⁴ <https://sncosmo.readthedocs.io>

Table 1: Color term coefficients for all filters using Emcee along with extinction coefficients.

Filter	B	V	R	I	Andicam Y	Andicam J	Andicam H	SOFI J	SOFI H	SOFI K_s
Color ^a	$B - V$	$B - V$	$R - I$	$R - I$	$z - Y$	$J - H$	$J - H$	$J - H$	$J - H$	$H - K_s$
Color term coefficient	0.079	-0.063	0.126	0.001	-0.997	0.113	-0.109	0.095	-0.179	-0.464
Color term error ^b	0.003	0.001	0.001	0.001	0.147	0.009	0.011	0.015	0.018	0.037
Extinction coefficient	0.251	0.149	0.098	0.066	0.007	0	0	0	0	0

Notes.

(^a) This refers to the catalog magnitude color used to determine the color term for a given filter. For example, $(B - V)_{cat}$ was used to determine the B -band color term coefficient.

(^b) Errors correspond to the 16th and 84th quantile, extinction coefficients were assumed to be 0 for the NIR filters

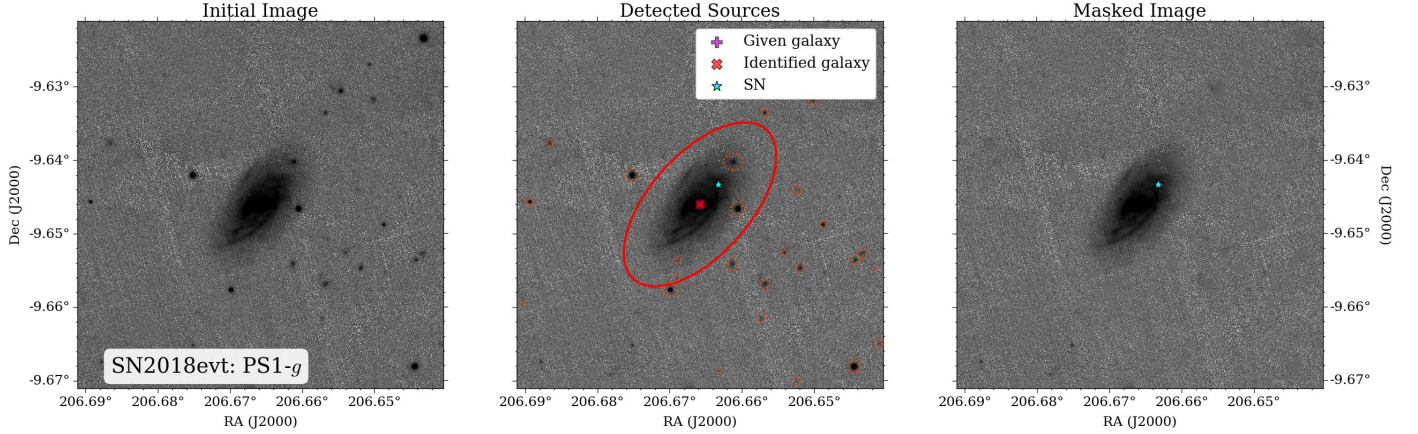


Fig. 10: Example of masking out stars using HostPhot. *Left*: Initial image downloaded from Pan-STARRS. *Middle*: Objects detected in HostPhot along with their apertures. *Right*: Image with sources removed.

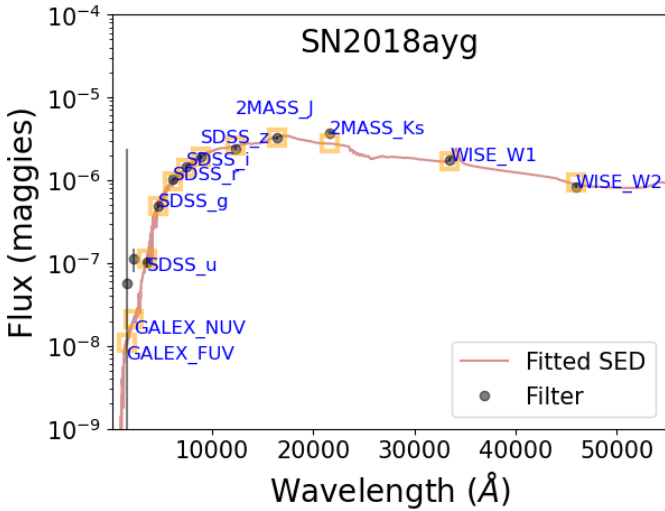


Fig. 11: Example of SED fitting in Prospector. Black points are the flux (in maggies) for our survey images. The fitted SED profile is marked in brown, and the yellow boxes indicate the model value for a given survey. Notice this is the initially detected aperture, not the final aperture measured by HostPhot.

but when combining the two, the B -band fit would be overestimated by 0.2 – 0.3 magnitudes with respect to the data, which was not seen in SNooPy and BayeSN. Also, the same problems were present when using the SALT2 template instead. We

checked the literature to see if some of our objects were observed by other telescopes. SN 2018aoz was studied by Ni et al. (2022) (see their supplementary Figure 3) and include B -band light curves with three different instruments (Korea Microlensing Telescope Network – KMTNet, Las Cumbres Observatory, and Swift Observatory). The SN peaked with an apparent magnitude of $B_{max} = 12.43 \pm 0.08$ mag (corrected for Milky Way extinction), which is in agreement with our results of 12.47 ± 0.07 , while ATLAS-only data would predict that the SN peaks at 12.7 mag. Because our data agrees with three other observatories, we therefore chose to exclude the ATLAS data whenever ANDICAM and ATLAS were incompatible.

Figure E.1 shows an example of light-curve fitting using SALT3-NIR along with BayeSN and SNooPy. From the output, we used SOURCE_PEAKMAG to determine the peak BJH -band apparent magnitudes corrected for Milky Way extinction.

5.2. SNooPy

SNooPy (Burns et al. 2014) is a Python-based tool for modeling and analyzing Type Ia supernova photometry, calibrated using high-quality CSP light curves and templates in the $uBVgriYJH$ filters. SNooPy has two different parametrizations for the shape of the light-curves: Δm_{15} , which is the average decline 15 days after peak brightness when fitting all bandpasses, and the color-stretch parameter s_{BV} (Burns et al. 2015), which measures the timing of the $B - V$ peak with respect to the average time of 30 days past B -band maximum. For the light-curve fitting, we used the MAX_MODEL, which fits the maximum magnitude for each filter individually and does K -corrections as well as a Milky Way

extinction correction. The fitted model is of the form

$$m_X = T_Y(t', \Delta m_{15}) + m_Y + R_X E(B - V)_{gal} + K_{X,Y}, \quad (11)$$

where T_Y is the light curve template, m_X is the observed magnitude in filter X , t' is the de-redshifted time relative to B -maximum, Δm_{15} is the decline rate parameter, m_Y is the peak magnitude in filter Y , R_X is the total-to-selective absorptions for filters X and $K_{X,Y}$ is the cross-band K -correction from rest-frame X to observed filter Y . The output from using `MAX_MODEL` gives multiple maxima transformed into the CSP filter systems along with time of maxima and s_{BV} or Δm_{15} .

For the ANDICAM I -band photometry, we noticed that `SNOOPY` had a tendency to overestimate the secondary peak for most of our SNe while underestimates the first peak. This issue was also seen in [Wee et al. \(2018\)](#), who also found this trend in the light curve of SN 2017cbv, a nearby object ($z \approx 0.004$). Since the I -band light curves were still able to reduce the uncertainties in the fitted LC parameters, the I -band light curves were still included.

5.3. BayeSN

`BAYESN`²⁵ ([Mandel et al. 2021](#); [Grayling et al. 2024](#)) is a hierarchical Bayesian model for SNe Ia SEDs that is continuous over time and wavelength, ranging from the optical to NIR, and the SED is modelled as a combination of distinct host galaxy dust and intrinsic spectral components. We used the [Ward et al. \(2023\)](#) model, which had been trained on the Foundation DR1 compilation ([Foley et al. 2017](#); [Jones et al. 2019](#)) and with [Avelino et al. \(2019\)](#) in the NIR. The training data includes *BgVrizYJH* filters, ranging from 3000-18500 Å. Input parameters are the time of observation, flux/magnitude, flux error/magnitude error, a Milky Way color excess, and redshift. The output of `BAYESN` gives a global distance modulus and time of peak maximum along with their errors. From the fits, obtained the peak magnitudes in each band (not corrected for extinction). The fitting results using the three fitters are reported in Table C.1 of the Appendix. Figure 12 shows the difference in B_{max} for the three light curve fitters. It is seen that `BayeSN` gives brighter B_{max} compared to `SNOOPY` with most points lying above zero, whereas the SNe for `SNOOPY` versus `SALT` are more evenly distributed around 0, and the same is true for `BayeSN` versus `SALT`. Our final SN light-curves are shown in Appendix D along with ZTF and ATLAS photometry.

6. Host galaxy masses

It was shown that there is a correlation between the optical brightness of SNe Ia and the host mass of the SN ([Kelly et al. 2010](#); [Sullivan et al. 2010](#); [Lampeitl et al. 2010](#)), where SNe found in massive galaxies were intrinsically brighter after standardization compared to SNe found in galaxies with low masses. To obtain more accurate distance measurements of the SNe, it is therefore important to take this “mass-step” into account. In this section we describe how to determine the host galaxy masses for our SNe.

6.1. Host galaxy photometry

Low resolution spectral energy distributions (SEDs) of the host galaxies at various wavelengths were constructed using the Python package `HOSTPHOT`²⁶ ([Müller-Bravo & Galbany 2022](#)).

Only using the SN redshift and the host galaxy coordinates, `HostPhot` downloads images in various filters from several surveys archives, such as GALEX, Pan-STARRS, DES, 2MASS, and unWISE. We then calculated the global apparent magnitude of the host and at the local environment of the SN within certain physical aperture (e.g. 2 kpc diameter using a flat Λ CDM cosmology with Hubble constant of $H_0 = 70 \text{ km s}^{-1} \text{ Mpc}^{-1}$ and matter density parameter $\Omega_{m0} = 0.3$ as default) in all those filters. Before computing photometry, nearby foreground stars were masked out, which would otherwise cause the brightness of the galaxy to be overestimated. An example of this masking is seen in Figure 10. We defined elliptical apertures and computed global host galaxy photometry for all SNe in our sample, as well as local 1-2-3 kpc circular aperture photometry centered at the SN location.

6.2. Host galaxy properties

`Prospector` ([Leja et al. 2017](#); [Johnson et al. 2021](#)) is a Python module for infer ring stellar population parameters from photometry and spectroscopy ranging from ultraviolet to infrared wavelengths. It is based on forward modeling the data (i.e. predict observational data by creating a theoretical model based on known physical principles) and Monte Carlo sampling the posterior parameter distribution, which enables complex models and exploration of moderate dimensional parameter spaces. Furthermore, `Prospector` uses the `FSPS` code ([Conroy et al. 2009](#); [Conroy & Gunn 2010](#)), which allowed us derive spectra of stellar populations. `Emcee` was used to obtain the posterior distributions of our host parameters, and for star formation history (SFH), a non-parametric SFH was used, which divides the galaxy’s lifetime into a series of time bins and estimates the star formation rate (SFR) in each bin independently. More specifically, the “continuity SFH” was chosen, which, as described in ([Leja et al. 2019](#)), allowed us to obtain a piecewise constant SFH without any sharp transitions in the SFH as function of time. In order to obtain recent values in SFH, the first two bins were fixed between 0-30 Myr and 30-100 Myr, and the oldest time bin was fixed to $0.9t_{univ}$, where t_{univ} is the age of the Universe (we assumed a flat Λ CDM universe with $\Omega_{m0} = 0.3$ and $H_0 = 70 \text{ km/s/Mpc}$, which is the same as for the light curve fitters) at a given observed redshift. The remaining bins were equally spaced in time logarithmically between 100Myr and $0.9t_{univ}$. Finally, the initial mass function from ([Kroupa 2002](#)) was used, which is a broken power law with an exponent of -0.3 for $0.01 < m/M_\odot < 0.08$, -1.3 for $0.08 < m/M_\odot < 0.5$, and -2.3 at $0.5 < m/M_\odot < 100$. To run `Prospector`, one needed the galaxy SEDs from `HostPhot` and the redshift (held fixed). To avoid overfitting and reduce the computing time, only one filter for each wavelength regime was be used (in other words, only one r -band was selected if there were multiple r -band filters available). So, for the optical regime, we prioritized, based on how deep the surveys went and the number of filters, DES, SDSS, PanSTARRS, Legacy Survey and SkyMapper, in this order. In those cases where the galaxy was too faint and result in negative fluxes (but consistent with 0), the flux was set to zero and the uncertainty to the 1-sigma upper limit, as suggested in the `Prospector` documentation²⁷. In the case of NIR data, the prioritization was UKIDSS, VISTA and 2MASS. Finally, for the mid-infrared data from unWISE, only the W1 ($\lambda_{mean} = 33526 \text{ Å}$) and W2 ($\lambda_{mean} = 46028 \text{ Å}$) filters were used, as the images in the far-infrared usually had very low resolution. Figure 11 shows an example of SED fitting using

²⁵ <https://github.com/bayesn/bayesn>

²⁶ <https://hostphot.readthedocs.io/en/latest/>

²⁷ <https://prospect.readthedocs.io/en/latest/faq.html>

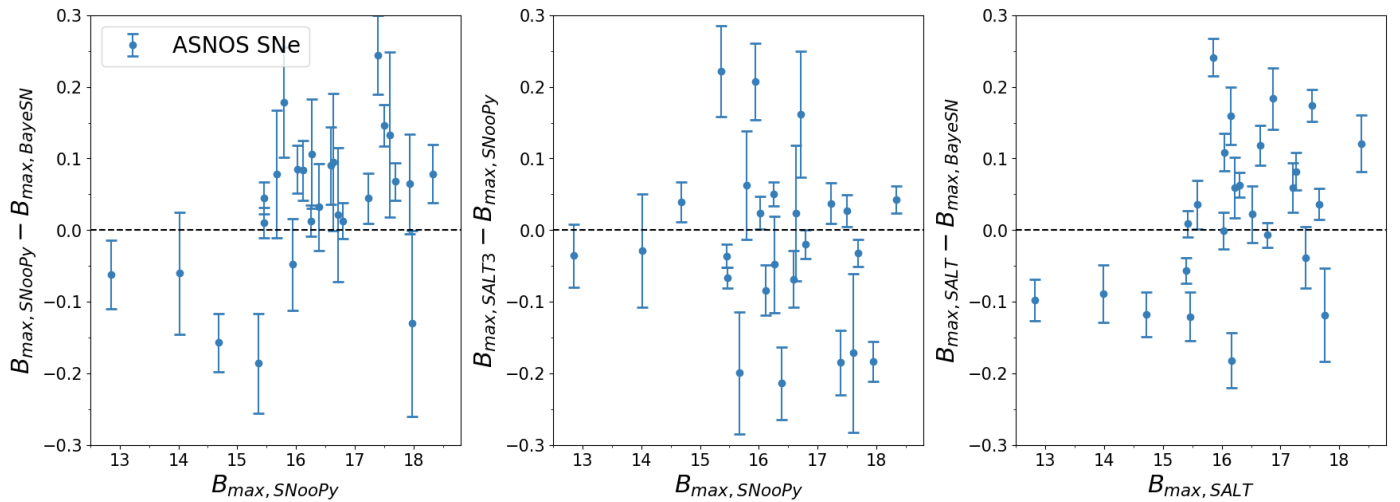


Fig. 12: Comparison of B_{\max} estimates from BayeSN, SALT3-NIR, and SNooPy. The light-curve fitters generally agree within ~ 0.1 mag on average. However, BayeSN yields systematically brighter B_{\max} values compared to SNooPy, with most SNe lying above zero. However, the SNe in the SALT3-NIR versus SNooPy appear to be evenly distributed around zero, and the same is true for SALT3-NIR versus BayeSN.

Prospector for the host galaxy of SN 2018ayg LEDA 1573011. The global photometry from HostPhot as well as the Prospector parameters can be seen in Table B.1, while the local photometry can be seen in Table B.2.

7. Summary and conclusion

In this paper, we presented SMARTS-ANDICAM optical and NIR data for 41 SNe, complemented by NTT-SOFI NIR imaging and described the data reduction and analysis procedures in detail. Given the significantly lower number of publicly available NIR observations of SNe (~ 300) compared to optical (~ 6000), the ASNOS sample increases by approximately 10% of the current NIR SN Ia dataset.

The photometry of the ANDICAM NIR images could have been significantly improved if our standard stars had been more consistent with one another when observed at the same night, which, as demonstrated by Figure 8, was not the case. Instead, we had to rely on faint local sequence stars within a limited field of view (FoV) of only 2.4×2.4 arcmin, with only 3 – 4 stars available to determine the image zeropoint using the catalog magnitudes from ATLAS-REFCAT2. Ideally, template images for subtraction would have been taken with the same instrument after the SN had faded. However, as the ANDICAM instrument was decommissioned in 2019, this was not possible. Additionally, the SOFI instrument ceased operation around 2023, just as our plan was to acquire template images, so archival data from different instruments had to be used instead. We also observed differences in color-term determinations from broad-band photometry as compared to synthetic photometry computed using the CALSPEC spectrophotometric standards. However, since the color term coefficients remained small in both cases, the impact on the apparent magnitudes of the SNe is minimal.

The resulting light curves were fitted using the three most widely used methods: SNCosmo with the SALT3-NIR template, SNooPy, and BayeSN. Finally, HOSTPHOT was used to derive spectral energy distributions (SEDs) of the host galaxies and local environments, and we employed Prospector to perform stellar population synthesis and estimate key galaxy parameters. After applying standard light-curve selection cuts, a final sample of

approximately 20 SNe with NIR observations was retained. This first paper serves as a description of the data reduction process and a data release, reporting all light-curve parameters and host galaxy masses. In a subsequent paper, we will combine literature SNe with our ANDICAM sample to measure extragalactic SN distances, construct Hubble diagrams, analyze differences between optical and NIR observations, and explore correlations between NIR Hubble residuals and host galaxy properties using various techniques such as host galaxy mass and specific star formation rate.

Data Availability

Tables and data will only be available in electronic form at the CDS via anonymous ftp to cdsarc.u-strasbg.fr (130.79.128.5) or via <http://cdsweb.u-strasbg.fr/cgi-bin/qcat?J/A+A/>.

Acknowledgements. The SNICE group acknowledges financial support from the Spanish Ministerio de Ciencia e Innovación (MCIN) and the Agencia Estatal de Investigación (AEI) 10.13039/501100011033 under the PID2020-115253GA-I00 HOSTFLOWS and the PID2023-151307NB-I00 SNNEXT projects, from Centro Superior de Investigaciones Científicas (CSIC) under projects PIE 20215AT016, ILINK23001, and the program Unidad de Excelencia María de Maeztu CEX2020-001058-M, and from the Departament de Recerca i Universitats de la Generalitat de Catalunya through the 2021-SGR-01270 grant. We acknowledge the financial support from the María de Maeztu Thematic Core at ICE-CSIC. S. Bose, M.D. Stritzinger, C. Soerensen, and the Aarhus-Barcelona FLOWS project are funded by the Independent Research Fund Denmark (IRFD, grant number 10.46540/2032-00022B) and by an Aarhus University Research Foundation Nova project (AUFF-E-2023-9-28).

This research has used data from the SMARTS 1.3-m telescope, which is operated as part of the SMARTS Consortium. Based on observations at NSF Cerro Tololo Inter-American Observatory, NSF NOIRLab (NOIRLab Prop. ID NOAO-18A-0047; NOAO-18B-0016; NOAO-19A-0081; PI: L. Galbany; and ID 2025A-754097; PI: K. Phan), which is managed by the Association of Universities for Research in Astronomy (AURA) under a cooperative agreement with the U.S. National Science Foundation. This work is based (in part) on observations collected at the European Organisation for Astronomical Research in the Southern Hemisphere, Chile as part of PESSTO, (the Public ESO Spectroscopic Survey for Transient Objects Survey) ESO program 188.D-3003, 191.D-0935, 197.D-1075. This research has made use of the NASA/IPAC Extragalactic Database (NED), which is operated by the Jet Propulsion Laboratory, California Institute of Technology, under contract with the National Aeronautics and Space Administration. This research has made use of the SIMBAD database, operated at CDS, Strasbourg, France. This research made use of Astropy, a community-developed core

Python package for Astronomy (Astropy Collaboration et al. 2018), as well as Photutils (Bradley et al. 2025).

References

- Abbott, T. M. C., Adamów, M., Agüena, M., et al. 2021, The Astrophysical Journal Supplement Series, 255, 20
- Astropy Collaboration, Price-Whelan, A. M., Sipőcz, B. M., et al. 2018, AJ, 156, 123
- Avelino, A., Friedman, A. S., Mandel, K. S., et al. 2019, The Astrophysical Journal, 887, 106
- Barbary, K., Bailey, S., Barentsen, G., et al. 2025, SNCosmo
- Barone-Nugent, R. L., Lidman, C., Wytke, J. S. B., et al. 2012, MNRAS, 425, 1007
- Bellm, E. C., Kulkarni, S. R., Graham, M. J., et al. 2018, Publications of the Astronomical Society of the Pacific, 131, 018002
- Bradley, L., Sipőcz, B., Robitaille, T., et al. 2025, astropy/photutils: 2.2.0
- Burns, C. R., Stritzinger, M., Phillips, M. M., et al. 2014, ApJ, 789, 32
- Burns, C. R., Stritzinger, M., Phillips, M. M., et al. 2015, SNoopy: TypeIa supernovae analysis tools
- Cardelli, J. A., Clayton, G. C., & Mathis, J. S. 1989, ApJ, 345, 245
- Chambers, K. C., Magnier, E. A., Metcalfe, N., et al. 2019, The Pan-STARRS1 Surveys
- Conroy, C. & Gunn, J. E. 2010, ApJ, 712, 833
- Conroy, C., Gunn, J. E., & White, M. 2009, ApJ, 699, 486
- Contreras, C., Hamuy, M., Phillips, M. M., et al. 2010, The Astronomical Journal, 139, 519–539
- DePoy, D. L., Atwood, B., Belville, S. R., et al. 2003, in Society of Photo-Optical Instrumentation Engineers (SPIE) Conference Series, Vol. 4841, Instrument Design and Performance for Optical/Infrared Ground-based Telescopes, ed. M. Iye & A. F. M. Moorwood, 827–838
- DES Collaboration, Abbott, T. M. C., Acevedo, M., et al. 2024, The Dark Energy Survey: Cosmology Results With 1500 New High-redshift Type Ia Supernovae Using The Full 5-year Dataset
- Do, A., Shappee, B. J., Tonry, J. L., et al. 2024, Monthly Notices of the Royal Astronomical Society, 536, 624–663
- Fitzpatrick, E. L. 1999, PASP, 111, 63
- Foley, R. J., Scolnic, D., Rest, A., et al. 2017, Monthly Notices of the Royal Astronomical Society, 475, 193–219
- Friedman, A. S., Wood-Vasey, W. M., Marion, G. H., et al. 2015, ApJS, 220, 9
- Galbany, L. 2020, in XIV.0 Scientific Meeting (virtual) of the Spanish Astronomical Society, 37
- Galbany, L., de Jaeger, T., Riess, A. G., et al. 2023, A&A, 679, A95
- Grayling, M., Thorp, S., Mandel, K. S., et al. 2024, Scalable hierarchical BayesN inference: Investigating dependence of SN Ia host galaxy dust properties on stellar mass and redshift
- Gupta, R. R., Kuhlmann, S., Kovacs, E., et al. 2016, The Astronomical Journal, 152, 154
- Hillebrandt, W. & Niemeyer, J. C. 2000, ARA&A, 38, 191
- Hsiao, E. Y., Phillips, M. M., Marion, G. H., et al. 2019, PASP, 131, 014002
- Jha, S. W., Avelino, A., Burns, C., et al. 2019, Supernovae in the Infrared with Hubble, HST Proposal. Cycle 27, ID. #15889
- Johansson, J., Cenko, S. B., Fox, O. D., et al. 2021, ApJ, 923, 237
- Johnson, B. D., Leja, J., Conroy, C., & Speagle, J. S. 2021, The Astrophysical Journal Supplement Series, 254, 22
- Johnson, B. D., Leja, J., Conroy, C., & Speagle, J. S. 2021, ApJS, 254, 22
- Jones, D. O., Mandel, K. S., Kirshner, R. P., et al. 2022, The Astrophysical Journal, 933, 172
- Jones, D. O., Scolnic, D. M., Foley, R. J., et al. 2019, The Astrophysical Journal, 881, 19
- Kashi, A. & Soker, N. 2011, MNRAS, 417, 1466
- Kelly, P. L., Hicken, M., Burke, D. L., Mandel, K. S., & Kirshner, R. P. 2010, The Astrophysical Journal, 715, 743–756
- Kenworthy, W. D., Jones, D. O., Dai, M., et al. 2021, The Astrophysical Journal, 923, 265
- Krisciunas, K., Contreras, C., Burns, C. R., et al. 2017, AJ, 154, 211
- Krisciunas, K., Phillips, M. M., & Suntzeff, N. B. 2004, The Astrophysical Journal, 602, L81–L84
- Kroupa, P. 2002, Science, 295, 82
- Kushnir, D., Katz, B., Dong, S., Livne, E., & Fernández, R. 2013, ApJ, 778, L37
- Lampeitl, H., Nichol, R. C., Seo, H.-J., et al. 2010, Monthly Notices of the Royal Astronomical Society, 401, 2331–2342
- Leja, J., Carnall, A. C., Johnson, B. D., Conroy, C., & Speagle, J. S. 2019, ApJ, 876, 3
- Leja, J., Johnson, B. D., Conroy, C., van Dokkum, P. G., & Byler, N. 2017, ApJ, 837, 170
- Livio, M. & Riess, A. G. 2003, ApJ, 594, L93
- Mandel, K. S., Thorp, S., Narayan, G., Friedman, A. S., & Avelino, A. 2021, Monthly Notices of the Royal Astronomical Society, 510, 3939–3966
- Müller-Bravo, T. & Galbany, L. 2022, The Journal of Open Source Software, 7, 4508
- Müller-Bravo, T. E., Galbany, L., Karamahmetoglu, E., et al. 2022, A&A, 665, A123
- Ni, Y. Q., Moon, D.-S., Drout, M. R., et al. 2022, Nature Astronomy, 6, 568–576
- Perlmutter, S., Aldering, G., Goldhaber, G., et al. 1999, The Astrophysical Journal, 517, 565–586
- Persson, S. E., Murphy, D. C., Smee, S., et al. 2013, PASP, 125, 654
- Peterson, E. R., Jones, D. O., Scolnic, D., et al. 2023, Monthly Notices of the Royal Astronomical Society, 522, 2478–2494
- Phillips, M. M. 1993, ApJ, 413, L105
- Phillips, M. M., Contreras, C., Hsiao, E. Y., et al. 2019, PASP, 131, 014001
- Pierel, J. D. R., Jones, D. O., Kenworthy, W. D., et al. 2022, The Astrophysical Journal, 939, 11
- Pskovskii, I. P. 1977, Soviet Ast., 21, 675
- Riess, A. G., Filippenko, A. V., Challis, P., et al. 1998, The Astronomical Journal, 116, 1009–1038
- Riess, A. G., Press, W. H., & Kirshner, R. P. 1996, ApJ, 473, 88
- Riess, A. G., Yuan, W., Macri, L. M., et al. 2022, ApJ, 934, L7
- Rigault, M., Smith, M., Goobar, A., et al. 2024, ZTF SN Ia DR2: Overview
- Rigault, M., Smith, M., Goobar, A., et al. 2025, A&A, 694, A1
- Sako, M., Bassett, B., Becker, A. C., et al. 2018, Publications of the Astronomical Society of the Pacific, 130, 064002
- Schlegel, D. J., Finkbeiner, D. P., & Davis, M. 1998, The Astrophysical Journal, 500, 525–553
- Scolnic, D., Brout, D., Carr, A., et al. 2022, The Astrophysical Journal, 938, 113
- Smartt, S. J., Valenti, S., Fraser, M., et al. 2015, A&A, 579, A40
- Stanishev, V., Goobar, A., Amanullah, R., et al. 2018, A&A, 615, A45
- Stritzinger, M., Suntzeff, N. B., Hamuy, M., et al. 2005, PASP, 117, 810
- Stritzinger, M. D., Phillips, M. M., Boldt, L. N., et al. 2011, The Astronomical Journal, 142, 156
- Sullivan, M., Conley, A., Howell, D. A., et al. 2010, Monthly Notices of the Royal Astronomical Society, no
- Sullivan, M., Le Borgne, D., Pritchett, C. J., et al. 2006, The Astrophysical Journal, 648, 868–883
- Thompson, T. A. 2011, The Astrophysical Journal, 741, 82
- Tonry, J. L., Denneau, L., Flewelling, H., et al. 2018, ApJ, 867, 105
- Tonry, J. L., Denneau, L., Heinze, A. N., et al. 2018, Publications of the Astronomical Society of the Pacific, 130, 064505
- Tonry, J. L., Stubbs, C. W., Lykke, K. R., et al. 2012, The Astrophysical Journal, 750, 99
- Tripp, R. 1998, A&A, 331, 815
- Wang, L., Contreras, C., Hu, M., et al. 2020, The Astrophysical Journal, 904, 14
- Ward, S. M., Thorp, S., Mandel, K. S., et al. 2023, ApJ, 956, 111
- Webbink, R. F. 1984, ApJ, 277, 355
- Wee, J., Chakraborty, N., Wang, J., & Penprase, B. E. 2018, The Astrophysical Journal, 863, 90
- Weyant, A., Wood-Vasey, W. M., Joyce, R., et al. 2018, AJ, 155, 201
- Whelan, J. & Iben, Jr., I. 1973, ApJ, 186, 1007
- Young, D. R. 2020

Appendix A: Supernova sample

Table A.1: SN types, coordinates, redshifts, host names, discovery and classification groups and number of observations in the NIR.

SN	Type	RA	Dec	z	Host name	Disc.	Class.	Total	Epochs ^(a)					
									ANDICAM			SOFI		
									Y	J	H	J _s	H _s	K _s
2018rw	Ia	06:09:39.200	-33:35:23.24	0.037052	FRL 1138	ASAS-SN	ePESSTO	7	0	6	1	0	0	0
2018yu	Ia	05:22:32.371	-11:29:13.86	0.009150	NGC 1888	DLT40	Zhang+	32	0	16	16	0	0	0
2018agk	Ia	13:10:36.373	-04:29:08.67	0.026131	IC 0855	Rest+	ASAS-SN	20	0	4	4	4	4	4
2018aoz	Ia	11:51:01.810	-28:44:38.69	0.005767	NGC 3923	DLT40	GSP	40	0	20	20	0	0	0
2018ayg	Ia	14:43:39.091	+18:52:12.51	0.030955	LEDA 1573011	ASAS-SN	Asiago	4	0	2	2	0	0	0
2018bie	Ia-91T	12:35:44.330	-00:13:16.43	0.023133	CGCG 014-073	ATLAS	ePESSTO	30	0	15	15	0	0	0
2018bta	Ia	16:57:58.670	-62:43:54.05	0.019691	ESO 101- G 020	BOSS	ePESSTO	28	0	14	14	0	0	0
2018cow	Ic-BL	16:16:00.220	+22:16:04.91	0.014060	2MASX J16160054+2216080	ATLAS	ZTF	22	0	11	11	0	0	0
2018dda	Ia	22:08:14.148	-25:03:41.21	0.018405	ESO 532- G 021	ASAS-SN	USC	39	13	13	13	0	0	0
2018ebu	Ia	21:57:19.870	-45:34:39.29	0.061	LEDA 525236	ASAS-SN	ATEL11894	17	0	7	7	1	1	1
2018enc	Ia	15:19:28.620	-09:52:49.94	0.023890	LEDA 985222	ATLAS	ePESSTO	30	7	7	7	3	3	3
2018eov	Ia	16:15:17.420	-61:07:53.54	0.016508	2MFGC 13057	GaiaAlerts	ePESSTO	30	7	7	7	3	3	3
2018evt	Ia-CSM	13:46:39.181	-09:38:36.00	0.025352	MCG -01-35-011	ASAS-SN	PESSTO	51	17	17	17	0	0	0
2018exb	Ia-91T	21:13:08.580	-20:42:38.77	0.047406	2MASX J21130828-2042398	ATLAS	Dong+	21	3	3	3	4	4	4
2018exc	Ia	21:00:08.018	-40:21:30.94	0.050575	2MFGC 15903	ATLAS	ePESSTO	30	5	5	5	5	5	5
2018feq	Ia-91T	01:15:18.506	-44:55:09.95	0.031505	ESO 244- G 007	ASAS-SN	ePESSTO	18	3	3	3	3	3	3
2018hfp	Ia	20:59:47.870	-16:38:12.52	0.029037	MCG -03-53-015	ASAS-SN	USC	42	12	12	12	2	2	2
2018hgc	Ia	00:42:04.605	-02:37:44.75	0.051782	LEDA 1086813	ASAS-SN	USC	45	13	13	13	2	2	2
2018hhn	Ia	22:52:32.100	+11:40:26.62	0.029313	UGC 12222	PSH	QUB	42	12	12	12	2	2	2
2018hjh	Ia-91T	07:53:02.180	+07:16:35.04	0.039316	CGCG 030-025	ASAS-SN	ePESSTO	39	12	12	12	1	1	1
2018ilu	Ia	23:33:20.969	+04:48:34.74	0.018070	SDSS J233320.80+044839.0	ATLAS	PESSTO	39	12	12	12	1	1	1
2018jag	Ia-91bg	01:03:48.310	+10:35:32.38	0.040657	MCG +02-03-030	TNTS	SCAT	42	13	13	13	1	1	1
2018jky	Ia	03:26:02.140	-17:33:46.44	0.014503	NGC 1329	ASAS-SN	GSP	39	12	12	12	1	1	1
2019gf	Ia-91T	08:05:35.263	-09:34:56.06	0.068469	-	ATLAS	ePESSTO	39	12	12	12	1	1	1
2019jf	Ia	08:36:14.793	-05:21:02.02	0.041382	2MASX J08361402-0521041	ATLAS	ePESSTO	39	12	12	12	1	1	1
2019rm	Ia	05:53:13.270	-73:06:56.74	0.023	2MASX J05531375-7306576	ASAS-SN	ePESSTO	36	11	11	11	1	1	1
2019so	Ia-91bg	12:42:36.420	-40:44:46.79	0.013747	NGC 4622	ATLAS	ePESSTO	47	15	15	15	1	1	0
2019ahi	Ia	13:51:36.599	-08:50:24.29	0.028763	LEDA 170305	ATLAS	QUB	3	1	1	1	0	0	0
2019akg	Ia-91T	10:45:03.732	+00:06:16.37	0.039798	UGC 05867	ATLAS	SCAT	39	12	12	12	1	1	1
2019awq	Ia	04:23:29.390	-15:46:00.55	0.036709	LEDA 146227	ATLAS	Cartier+	48	14	14	14	2	2	2
2019bdz	Ia	14:48:36.894	+06:48:51.93	0.034632	CGCG 048-018	ATLAS	Asiago	45	14	14	14	1	1	1
2019bus	Ia-91T	14:29:25.706	+16:40:55.42	0.082326	LEDA 1514443	ATLAS	ePESSTO	27	9	9	9	0	0	0
2019cvi	Ia	19:32:22.129	-29:23:08.31	0.023833	MCG -05-46-002	ASAS-SN	SCAT	39	13	13	13	0	0	0
2019cxu	Ia-02cx	13:05:30.082	-08:45:52.68	0.044014	-	ZTF	GSP	24	8	8	8	0	0	0
2019cxi	Ia	11:17:48.187	+13:43:41.55	0.024784	IC 2695	Tanaka+	Tanaka+	33	10	10	10	1	1	1
2019dks	Ia-91T	11:44:05.602	-04:40:25.21	0.060682	WISEA J114405.79-044026.4	ZTF	GSP	36	12	12	12	0	0	0
2019eim	Ia	23:49:42.938	-69:42:02.38	0.039	LEDA 277632	ASAS-SN	ePESSTO	33	11	11	11	0	0	0
2019fcf	Ia	17:40:17.630	+17:41:39.16	0.058425	LEDA 1539132	ATLAS	ePESSTO	33	11	11	11	0	0	0
2019fmr	Ia-91T	23:17:38.900	-59:15:42.77	0.026915	LEDA 372765	ASAS-SN	Stritzinger	30	10	10	10	0	0	0
2019gbx	Ia	12:50:02.812	-14:45:59.96	0.013146	MCG-02-33-017	ATLAS	Zhang+	57	19	19	19	0	0	0
2019gwa	Ia-91T	15:58:41.190	+11:14:25.04	0.054953	SDSS J155841.10+111425.5	ZTF	SCAT	45	15	15	15	0	0	0

Notes.

^(a) The number outside the parenthesis indicates the total number of NIR images, and the “s” subscript denotes SOFI filters.

Appendix B: Host galaxy parameters

Table B.1: Global photometry for our SN hosts using HostPhot along with host galaxy properties from Prospector.

SN	FUV	GALEX	NUV	u	v	g	r	Optical ^a	z	Y	J	NR	K_s	Survey	$W1$	unWISE	$W2$	$\log(M/M_\odot)$	$\log(Z_\odot)$	Prospector output ^b	$\log(SFR_{100})$	$\log(SFR_{250})$	$\log(SFR_{\text{gal}})$	d_{10}
2018ew	-	-	-	16.22 (0.16)	18.25 (0.80)	15.33 (0.01)	14.65 (0.01)	14.36 (0.01)	14.13 (0.13)	13.96 (0.01)	13.42 (0.02)	12.49 (0.02)	12.11 (0.03)	2MASS	11.20 (0.04)	11.12 (0.09)	11.12 (0.09)	10.72 ^{+0.04} _{-0.04}	-0.61 ^{+0.04} _{-0.04}	1.51 ^{+0.04} _{-0.04}	1.11 ^{+0.04} _{-0.04}	1.11 ^{+0.04} _{-0.04}	0.91 ^{+0.04} _{-0.04}	0.50
2018ya	-	-	-	15.47 (0.75)	-	12.67 (0.04)	11.87 (0.03)	11.87 (0.03)	10.86 (0.01)	-	9.86 (0.00)	9.14 (0.00)	8.85 (0.01)	2MASS	7.90 (0.03)	7.79 (0.04)	7.79 (0.04)	9.35 ^{+0.04} _{-0.04}	-0.72 ^{+0.04} _{-0.04}	1.76 ^{+0.04} _{-0.04}	1.38 ^{+0.04} _{-0.04}	1.38 ^{+0.04} _{-0.04}	1.16 ^{+0.04} _{-0.04}	0.67
2018bz	15.83 (13.92)	14.66 (0.10)	-	13.95 (0.35)	13.18 (0.23)	14.70 (0.01)	14.51 (0.01)	14.16 (0.02)	14.06 (0.02)	14.00 (0.02)	12.38 (0.00)	12.30 (0.00)	12.12 (0.02)	2MASS	10.63 (0.18)	10.63 (0.18)	10.63 (0.18)	9.94 ^{+0.04} _{-0.04}	-0.28 ^{+0.04} _{-0.04}	2.21 ^{+0.04} _{-0.04}	1.84 ^{+0.04} _{-0.04}	1.84 ^{+0.04} _{-0.04}	1.66 ^{+0.04} _{-0.04}	0.46
2018bz	14.39 (13.95)	17.36 (0.35)	-	17.36 (0.35)	-	15.79 (0.01)	14.98 (0.01)	14.59 (0.02)	14.50 (0.02)	8.96 (0.02)	13.14 (0.01)	12.31 (0.00)	7.10 (0.00)	SkyMapper-Pan-STARRS	6.18 (0.02)	6.18 (0.02)	6.18 (0.02)	10.51 ^{+0.04} _{-0.04}	-0.28 ^{+0.04} _{-0.04}	1.84 ^{+0.04} _{-0.04}	1.84 ^{+0.04} _{-0.04}	1.84 ^{+0.04} _{-0.04}	1.66 ^{+0.04} _{-0.04}	0.46
2018bz	17.66 (0.67)	15.92 (0.17)	-	17.24 (0.14)	-	16.33 (0.01)	15.88 (0.01)	15.63 (0.02)	15.45 (0.02)	15.38 (0.02)	13.90 (0.02)	13.34 (0.01)	11.97 (0.00)	2MASS	8.85 (0.05)	8.85 (0.05)	8.85 (0.05)	10.51 ^{+0.04} _{-0.04}	-0.28 ^{+0.04} _{-0.04}	1.84 ^{+0.04} _{-0.04}	1.84 ^{+0.04} _{-0.04}	1.84 ^{+0.04} _{-0.04}	1.66 ^{+0.04} _{-0.04}	0.46
2018bz	-	-	-	15.10 (0.13)	14.63 (0.10)	13.01 (0.02)	12.85 (0.02)	12.60 (0.01)	12.10 (0.02)	-	10.86 (0.01)	10.34 (0.01)	9.97 (0.00)	2MASS	12.97 (0.09)	12.97 (0.09)	12.97 (0.09)	8.91 ^{+0.04} _{-0.04}	-0.94 ^{+0.04} _{-0.04}	1.42 ^{+0.04} _{-0.04}	1.57 ^{+0.04} _{-0.04}	1.57 ^{+0.04} _{-0.04}	1.57 ^{+0.04} _{-0.04}	1.09
2018bz	-	-	-	15.30 (0.02)	14.63 (0.10)	13.01 (0.02)	12.85 (0.02)	12.60 (0.01)	12.10 (0.02)	-	10.86 (0.01)	10.34 (0.01)	9.97 (0.00)	VISTA	8.52 (0.03)	8.52 (0.03)	8.52 (0.03)	11.17 ^{+0.04} _{-0.04}	-0.77 ^{+0.04} _{-0.04}	1.73 ^{+0.04} _{-0.04}	1.34 ^{+0.04} _{-0.04}	1.34 ^{+0.04} _{-0.04}	1.14 ^{+0.04} _{-0.04}	0.88
2018bz	16.43 (17.84)	15.90 (0.21)	-	16.34 (0.10)	-	15.33 (0.05)	14.85 (0.04)	14.62 (0.03)	14.45 (0.03)	-	13.74 (0.01)	12.98 (0.02)	12.80 (0.03)	UKIDSS	8.52 (0.03)	8.52 (0.03)	8.52 (0.03)	9.18 ^{+0.04} _{-0.04}	-0.86 ^{+0.04} _{-0.04}	1.66 ^{+0.04} _{-0.04}	1.66 ^{+0.04} _{-0.04}	1.66 ^{+0.04} _{-0.04}	1.47 ^{+0.04} _{-0.04}	0.44
2018bz	16.19 (14.72)	15.31 (0.14)	-	-	-	14.27 (0.01)	13.70 (0.01)	13.44 (0.02)	13.02 (0.02)	-	12.00 (0.01)	11.20 (0.01)	10.22 ^{+0.04} _{-0.04}	VISTA	10.65 (0.06)	10.65 (0.06)	10.65 (0.06)	10.22 ^{+0.04} _{-0.04}	-0.29 ^{+0.04} _{-0.04}	1.67 ^{+0.04} _{-0.04}	1.29 ^{+0.04} _{-0.04}	1.29 ^{+0.04} _{-0.04}	1.09 ^{+0.04} _{-0.04}	0.21
2018bz	17.50 (29.40)	16.46 (0.22)	-	-	-	16.77 (0.01)	16.29 (0.01)	16.10 (0.01)	15.92 (0.01)	15.82 (0.01)	14.77 (0.01)	14.21 (0.01)	13.95 (0.02)	VISTA	13.51 (0.19)	13.51 (0.19)	13.51 (0.19)	10.22 ^{+0.04} _{-0.04}	-0.29 ^{+0.04} _{-0.04}	1.67 ^{+0.04} _{-0.04}	1.29 ^{+0.04} _{-0.04}	1.29 ^{+0.04} _{-0.04}	1.09 ^{+0.04} _{-0.04}	0.21
2018bz	-	-	-	-	-	16.75 (0.02)	16.58 (0.02)	16.50 (0.02)	16.47 (0.02)	16.36 (0.04)	-	15.40 (0.05)	14.66 (0.08)	VISTA	14.38 (0.14)	14.38 (0.14)	14.38 (0.14)	9.12 ^{+0.04} _{-0.04}	-0.85 ^{+0.04} _{-0.04}	1.66 ^{+0.04} _{-0.04}	1.27 ^{+0.04} _{-0.04}	1.27 ^{+0.04} _{-0.04}	1.07 ^{+0.04} _{-0.04}	1.30
2018bz	-	-	-	17.10 (0.90)	15.34 (0.61)	13.44 (0.02)	12.95 (0.02)	12.46 (0.02)	12.41 (0.02)	-	11.40 (0.05)	10.55 (0.16)	10.55 (0.16)	VISTA	11.07 (0.05)	11.07 (0.05)	11.07 (0.05)	10.81 ^{+0.04} _{-0.04}	-0.82 ^{+0.04} _{-0.04}	1.47 ^{+0.04} _{-0.04}	1.07 ^{+0.04} _{-0.04}	1.07 ^{+0.04} _{-0.04}	0.87 ^{+0.04} _{-0.04}	0.95
2018bz	17.85 (39.51)	16.60 (0.25)	-	16.35 (0.17)	-	16.05 (0.01)	15.37 (0.01)	15.01 (0.02)	14.77 (0.02)	14.61 (0.02)	13.70 (0.02)	12.40 (0.02)	11.95 (0.48)	VISTA	11.63 (0.05)	11.63 (0.05)	11.63 (0.05)	10.71 ^{+0.04} _{-0.04}	-0.26 ^{+0.04} _{-0.04}	1.48 ^{+0.04} _{-0.04}	1.16 ^{+0.04} _{-0.04}	1.16 ^{+0.04} _{-0.04}	1.03 ^{+0.04} _{-0.04}	0.82
2018bz	17.22 (24.43)	16.12 (0.18)	-	16.34 (0.28)	15.94 (0.26)	15.86 (0.13)	15.42 (0.08)	15.09 (0.07)	14.87 (0.07)	-	13.31 (0.01)	12.13 (0.01)	11.79 (0.01)	VISTA	11.09 (0.04)	11.09 (0.04)	11.09 (0.04)	10.38 ^{+0.04} _{-0.04}	-0.17 ^{+0.04} _{-0.04}	1.79 ^{+0.04} _{-0.04}	1.40 ^{+0.04} _{-0.04}	1.40 ^{+0.04} _{-0.04}	1.21 ^{+0.04} _{-0.04}	0.80
2018bz	14.67 (14.07)	14.95 (0.13)	-	14.67 (0.13)	-	14.11 (0.01)	13.49 (0.01)	13.18 (0.02)	12.98 (0.02)	12.65 (0.02)	12.77 (0.01)	12.13 (0.01)	11.79 (0.01)	VISTA	11.09 (0.04)	11.09 (0.04)	11.09 (0.04)	10.38 ^{+0.04} _{-0.04}	-0.17 ^{+0.04} _{-0.04}	1.79 ^{+0.04} _{-0.04}	1.40 ^{+0.04} _{-0.04}	1.40 ^{+0.04} _{-0.04}	1.21 ^{+0.04} _{-0.04}	0.80
2018bz	18.28 (0.93)	17.33 (0.34)	-	17.27 (0.14)	-	16.14 (0.07)	15.69 (0.05)	15.34 (0.04)	15.15 (0.04)	-	13.64 (0.01)	13.02 (0.02)	13.03 (0.03)	2MASS	12.26 (0.04)	12.26 (0.04)	12.26 (0.04)	10.51 ^{+0.04} _{-0.04}	-0.46 ^{+0.04} _{-0.04}	2.16 ^{+0.04} _{-0.04}	1.77 ^{+0.04} _{-0.04}	1.77 ^{+0.04} _{-0.04}	1.57 ^{+0.04} _{-0.04}	0.50
2018bz	15.84 (13.17)	15.03 (0.14)	-	15.10 (0.06)	-	13.90 (0.03)	13.27 (0.02)	12.95 (0.02)	12.70 (0.01)	-	14.12 (0.01)	13.37 (0.01)	12.51 (0.01)	UKIDSS	10.21 (0.02)	10.21 (0.02)	10.21 (0.02)	10.46 ^{+0.04} _{-0.04}	-0.57 ^{+0.04} _{-0.04}	1.44 ^{+0.04} _{-0.04}	1.44 ^{+0.04} _{-0.04}	1.44 ^{+0.04} _{-0.04}	1.44 ^{+0.04} _{-0.04}	1.21
2018bz	16.96 (17.56)	16.10 (0.19)	-	16.73 (0.11)	-	15.83 (0.06)	15.56 (0.05)	15.23 (0.04)	15.33 (0.05)	-	14.12 (0.01)	13.37 (0.01)	12.51 (0.01)	UKIDSS	10.21 (0.02)	10.21 (0.02)	10.21 (0.02)	10.46 ^{+0.04} _{-0.04}	-0.57 ^{+0.04} _{-0.04}	1.44 ^{+0.04} _{-0.04}	1.44 ^{+0.04} _{-0.04}	1.44 ^{+0.04} _{-0.04}	1.44 ^{+0.04} _{-0.04}	1.21
2018bz	19.16 (63.06)	18.50 (0.64)	-	19.96 (0.65)	-	19.39 (0.33)	19.17 (0.29)	18.91 (0.26)	18.78 (0.30)	-	18.29 (0.22)	17.50 (0.28)	17.52 (0.53)	UKIDSS	11.86 (0.03)	11.86 (0.03)	11.86 (0.03)	9.65 ^{+0.04} _{-0.04}	-0.75 ^{+0.04} _{-0.04}	1.98 ^{+0.04} _{-0.04}	1.60 ^{+0.04} _{-0.04}	1.60 ^{+0.04} _{-0.04}	1.40 ^{+0.04} _{-0.04}	1.36
2018bz	17.59 (43.75)	16.24 (0.2)	-	16.75 (0.12)	-	13.04 (0.01)	12.32 (0.03)	12.00 (0.01)	11.75 (0.01)	-	10.54 (0.01)	9.93 (0.01)	9.65 (0.01)	2MASS	9.30 (0.03)	9.30 (0.03)	9.30 (0.03)	10.75 ^{+0.04} _{-0.04}	-0.55 ^{+0.04} _{-0.04}	1.48 ^{+0.04} _{-0.04}	1.17 ^{+0.04} _{-0.04}	1.17 ^{+0.04} _{-0.04}	1.02 ^{+0.04} _{-0.04}	2.14
2018bz	15.87 (0.33)	15.13 (0.13)	-	21.06 (1.41)	-	20.64 (0.04)	20.16 (0.03)	20.00 (0.02)	20.06 (0.05)	-	16.10 (0.04)	17.26 (0.23)	-	2MASS	9.30 (0.03)	9.30 (0.03)	9.30 (0.03)	10.75 ^{+0.04} _{-0.04}	-0.55 ^{+0.04} _{-0.04}	1.48 ^{+0.04} _{-0.04}	1.17 ^{+0.04} _{-0.04}	1.17 ^{+0.04} _{-0.04}	1.02 ^{+0.04} _{-0.04}	2.14
2019gf	-	-	-	-	-	15.68 (0.01)	14.94 (0.01)	14.56 (0.02)	14.40 (0.02)	-	13.11 (0.01)	12.17 (0.01)	12.17 (0.01)	VISTA	11.16 (0.04)	11.16 (0.04)	11.16 (0.04)	10.84 ^{+0.04} _{-0.04}	-0.62 ^{+0.04} _{-0.04}	1.52 ^{+0.04} _{-0.04}	1.14 ^{+0.04} _{-0.04}	1.14 ^{+0.04} _{-0.04}	0.95 ^{+0.04} _{-0.04}	0.75
2019m	18.74 (142.02)	14.84 (124.77)	-	-	-	13.13 (0.08)	13.21 (0.08)	12.07 (0.03)	11.59 (0.02)	-	13.53 (0.03)	13.18 (0.05)	12.31 (0.04)	2MASS	10.81 (0.03)	10.81 (0.03)	10.81 (0.03)	9.39 ^{+0.04} _{-0.04}	-0.82 ^{+0.04} _{-0.04}	2.76 ^{+0.04} _{-0.04}	1.34 ^{+0.04} _{-0.04}	1.34 ^{+0.04} _{-0.04}	1.06 ^{+0.04} _{-0.04}	0.24
2019o	14.46 (5.85)	14.01 (0.11)	-	-	-	14.20 (0.01)	13.90 (0.01)	13.72 (0.02)	13.62 (0.02)	13.46 (0.02)	10.41 (0.01)	9.49 (0.01)	8.71 (0.04)	VISTA	8.71 (0.04)	8.71 (0.04)	8.71 (0.04)	11.01 ^{+0.04} _{-0.04}	-0.12 ^{+0.04} _{-0.04}	2.36 ^{+0.04} _{-0.04}	1.14 ^{+0.04} _{-0.04}	1.14 ^{+0.04} _{-0.04}	0.95 ^{+0.04} _{-0.04}	0.31
2019ah	15.75 (9.83)	14.88 (0.12)	-	-	-	14.68 (0.04)	14.14 (0.03)	13.82 (0.02)	13.61 (0.02)	-	12.74 (0.13)	11.93 (0.10)	11.64 (0.06)	VISTA	10.90 (0.06)	10.90 (0.06)	10.90 (0.06)	10.58 ^{+0.04} _{-0.04}	-0.44 ^{+0.04} _{-0.04}	1.35 ^{+0.04} _{-0.04}	1.13 ^{+0.04} _{-0.04}	1.13 ^{+0.04} _{-0.04}	1.02 ^{+0.04} _{-0.04}	0.65
2019awq	16.26 (0.39)	15.35 (0.15)	-	15.91 (0.08)	-	15.93 (0.01)	15.27 (0.01)	14.92 (0.02)	14.72 (0.02)	14.53 (0.02)	13.17 (0.01)	12.19 (0.01)	11.87 (0.02)	UKIDSS	11.05 (0.03)	11.05 (0.03)	11.05 (0.03)	10.68 ^{+0.04} _{-0.04}	-0.78 ^{+0.04} _{-0.04}	1.50 ^{+0.04} _{-0.04}	1.19 ^{+0.04} _{-0.04}	1.19 ^{+0.04} _{-0.04}	1.02 ^{+0.04} _{-0.04}	0.40
2019awq	15.77 (28.61)	16.98 (0.30)	-	17.69 (0.28)	-	15.18 (0.05)	14.71 (0.03)	14.42 (0.03)	14.24 (0.03)	-	13.51 (0.01)	13.14 (0.01)	12.80 (0.02)	UKIDSS	11.63 (0.04)	11.63 (0.04)	11.63 (0.04)	10.52 ^{+0.04} _{-0.04}	-0.72 ^{+0.04} _{-0.04}	1.39 ^{+0.04} _{-0.04}	1.08 ^{+0.04} _{-0.04}	1.08 ^{+0.04} _{-0.04}	0.94 ^{+0.04} _{-0.04}	0.77
2019bz	16.85 (21.61)	15.87 (0.18)	-	16.21 (0.08)	-	17.77 (0.14)	17.22 (0.11)	16.93 (0.10)	16.73 (0.09)	-	15.50 (0.03)	14.70 (0.02)	14.70 (0.02)	UKIDSS	11.58 (0.04)	11.58 (0.04)	11.58 (0.04)	9.94 ^{+0.04} _{-0.04}	-0.96 ^{+0.04} _{-0.04}	1.54 ^{+0.04} _{-0.04}	1.34 ^{+0.04} _{-0.04}	1.34 ^{+0.04} _{-0.04}	1.26 ^{+0.04} _{-0.04}	0.86
2019bz	19.44 (69.53)	18.71 (0.63)	-	17.69 (0.28)	-	13.35 (0.01)	13.02 (0.01)	12.82 (0.02)	12.69 (0.02)	12.37 (0.02)	11.36 (0.01)	10.49 (0.01)	9.71 (0.04)	VISTA	9.27 (0.06)	9.27 (0.06)	9.27 (0.06)	10.92 ^{+0.04} _{-0.04}	-0.84 ^{+0.04} _{-0.04}	1.59 ^{+0.04} _{-0.04}	1.39 ^{+0.04} _{-0.04}	1.39 ^{+0.04} _{-0.04}	1.26 ^{+0.04} _{-0.04}	0.70
2019bz	14.64 (0.25)	13.95 (0.10)	-	-	-	16.35 (0.07)	15.95 (0.06)	15.73 (0.05)	15.61 (0.05)	15.27 (0.11)	11.36 (0.01)	10.49 (0.01)	9.71 (0.04)	VISTA	9.27 (0.06)	9.27 (0.06)	9.27 (0.06)	10.92 ^{+0.04} _{-0.04}	-0.84 ^{+0.04} _{-0.04}					

Table B.2: Same as Table B.1 but with local photometry. For each filter we indicate the apparent magnitude inside apertures of 1, 2 and 3 kpc centered around the SN position. Note that in some cases it was not possible to measure any flux because there is no host light within the aperture.

SN	DATE	COIN	W1	W2	W3	W4	W5	W6	W7	W8	W9	W10	W11	W12	W13	W14	W15	W16	W17	W18	W19	W20	W21	W22	W23	W24	W25	W26	W27	W28	W29	W30	W31	W32	W33	W34	W35	W36	W37	W38	W39	W40	W41	W42	W43	W44	W45	W46	W47	W48	W49	W50	W51	W52	W53	W54	W55	W56	W57	W58	W59	W60	W61	W62	W63	W64	W65	W66	W67	W68	W69	W70	W71	W72	W73	W74	W75	W76	W77	W78	W79	W80	W81	W82	W83	W84	W85	W86	W87	W88	W89	W90	W91	W92	W93	W94	W95	W96	W97	W98	W99	W100	W101	W102	W103	W104	W105	W106	W107	W108	W109	W110	W111	W112	W113	W114	W115	W116	W117	W118	W119	W120	W121	W122	W123	W124	W125	W126	W127	W128	W129	W130	W131	W132	W133	W134	W135	W136	W137	W138	W139	W140	W141	W142	W143	W144	W145	W146	W147	W148	W149	W150	W151	W152	W153	W154	W155	W156	W157	W158	W159	W160	W161	W162	W163	W164	W165	W166	W167	W168	W169	W170	W171	W172	W173	W174	W175	W176	W177	W178	W179	W180	W181	W182	W183	W184	W185	W186	W187	W188	W189	W190	W191	W192	W193	W194	W195	W196	W197	W198	W199	W200	W201	W202	W203	W204	W205	W206	W207	W208	W209	W210	W211	W212	W213	W214	W215	W216	W217	W218	W219	W220	W221	W222	W223	W224	W225	W226	W227	W228	W229	W230	W231	W232	W233	W234	W235	W236	W237	W238	W239	W240	W241	W242	W243	W244	W245	W246	W247	W248	W249	W250	W251	W252	W253	W254	W255	W256	W257	W258	W259	W260	W261	W262	W263	W264	W265	W266	W267	W268	W269	W270	W271	W272	W273	W274	W275	W276	W277	W278	W279	W280	W281	W282	W283	W284	W285	W286	W287	W288	W289	W290	W291	W292	W293	W294	W295	W296	W297	W298	W299	W300	W301	W302	W303	W304	W305	W306	W307	W308	W309	W310	W311	W312	W313	W314	W315	W316	W317	W318	W319	W320	W321	W322	W323	W324	W325	W326	W327	W328	W329	W330	W331	W332	W333	W334	W335	W336	W337	W338	W339	W340	W341	W342	W343	W344	W345	W346	W347	W348	W349	W350	W351	W352	W353	W354	W355	W356	W357	W358	W359	W360	W361	W362	W363	W364	W365	W366	W367	W368	W369	W370	W371	W372	W373	W374	W375	W376	W377	W378	W379	W380	W381	W382	W383	W384	W385	W386	W387	W388	W389	W390	W391	W392	W393	W394	W395	W396	W397	W398	W399	W400	W401	W402	W403	W404	W405	W406	W407	W408	W409	W410	W411	W412	W413	W414	W415	W416	W417	W418	W419	W420	W421	W422	W423	W424	W425	W426	W427	W428	W429	W430	W431	W432	W433	W434	W435	W436	W437	W438	W439	W440	W441	W442	W443	W444	W445	W446	W447	W448	W449	W450	W451	W452	W453	W454	W455	W456	W457	W458	W459	W460	W461	W462	W463	W464	W465	W466	W467	W468	W469	W470	W471	W472	W473	W474	W475	W476	W477	W478	W479	W480	W481	W482	W483	W484	W485	W486	W487	W488	W489	W490	W491	W492	W493	W494	W495	W496	W497	W498	W499	W500	W501	W502	W503	W504	W505	W506	W507	W508	W509	W510	W511	W512	W513	W514	W515	W516	W517	W518	W519	W520	W521	W522	W523	W524	W525	W526	W527	W528	W529	W530	W531	W532	W533	W534	W535	W536	W537	W538	W539	W540	W541	W542	W543	W544	W545	W546	W547	W548	W549	W550	W551	W552	W553	W554	W555	W556	W557	W558	W559	W560	W561	W562	W563	W564	W565	W566	W567	W568	W569	W570	W571	W572	W573	W574	W575	W576	W577	W578	W579	W580	W581	W582	W583	W584	W585	W586	W587	W588	W589	W590	W591	W592	W593	W594	W595	W596	W597	W598	W599	W600	W601	W602	W603	W604	W605	W606	W607	W608	W609	W610	W611	W612	W613	W614	W615	W616	W617	W618	W619	W620	W621	W622	W623	W624	W625	W626	W627	W628	W629	W630	W631	W632	W633	W634	W635	W636	W637	W638	W639	W640	W641	W642	W643	W644	W645	W646	W647	W648	W649	W650	W651	W652	W653	W654	W655	W656	W657	W658	W659	W660	W661	W662	W663	W664	W665	W666	W667	W668	W669	W670	W671	W672	W673	W674	W675	W676	W677	W678	W679	W680	W681	W682	W683	W684	W685	W686	W687	W688	W689	W690	W691	W692	W693	W694	W695	W696	W697	W698	W699	W700	W701	W702	W703	W704	W705	W706	W707	W708	W709	W710	W711	W712	W713	W714	W715	W716	W717	W718	W719	W720	W721	W722	W723	W724	W725	W726	W727	W728	W729	W730	W731	W732	W733	W734	W735	W736	W737	W738	W739	W740	W741	W742	W743	W744	W745	W746	W747	W748	W749	W750	W751	W752	W753	W754	W755	W756	W757	W758	W759	W760	W761	W762	W763	W764	W765	W766	W767	W768	W769	W770	W771	W772	W773	W774	W775	W776	W777	W778	W779	W780	W781	W782	W783	W784	W785	W786	W787	W788	W789	W790	W791	W792	W793	W794	W795	W796	W797	W798	W799	W800	W801	W802	W803	W804	W805	W806	W807	W808	W809	W810	W811	W812	W813	W814	W815	W816	W817	W818	W819	W820	W821	W822	W823	W824	W825	W826	W827	W828	W829	W830	W831	W832	W833	W834	W835	W836	W837	W838	W839	W840	W841	W842	W843	W844	W845	W846	W847	W848	W849	W850	W851	W852	W853	W854	W855	W856	W857	W858	W859	W860	W861	W862	W863	W864	W865	W866	W867	W868	W869	W870	W871	W872	W873	W874	W875	W876	W877	W878	W879	W880	W881	W882	W883	W884	W885	W886	W887	W888	W889	W890	W891	W892	W893	W894	W895	W896	W897	W898	W899	W900	W901	W902	W903	W904	W905	W906	W907	W908	W909	W910	W911	W912	W913	W914	W915	W916	W917	W918	W919	W920	W921	W922	W923	W924	W925	W926	W927	W928	W929	W930	W931	W932	W933	W934	W935	W936	W937	W938	W939	W940	W941	W942	W943	W944	W945	W946	W947	W948	W949	W950	W951	W952	W953	W954	W955	W956	W957	W958	W959	W960	W961	W962	W963	W964	W965	W966	W967	W968	W969	W970	W971	W972	W973	W974	W975	W976	W977	W978	W979	W980	W981	W982	W983	W984	W985	W986	W987	W988	W989	W990	W991	W992	W993	W994	W995	W996	W997	W998	W999	W1000	W1001	W1002	W1003	W1004	W1005	W1006	W1007	W1008	W1009	W1010	W1011	W1012	W1013	W1014	W1015	W1016	W1017	W1018	W1019	W1020	W1021	W1022	W1023	W1024	W1025	W1026	W1027	W1028	W1029	W1030	W1031	W1032	W1033	W1034	W1035	W1036	W1037	W1038	W1039	W1040	W1041	W1042	W1043	W1044	W1045	W1046	W1047	W1048	W1049	W1050	W1051	W1052	W1053	W1054	W1055	W1056	W1057	W1058	W1059	W1060	W1061	W1062	W1063	W1064	W1065	W1066	W1067	W1068	W1069	W1070	W1071	W1072	W1073	W1074	W1075	W1076	W1077	W1078	W1079	W1080	W1081	W1082	W1083	W1084	W1085	W1086	W1087	W1088	W1089	W1090	W1091	W1092	W1093	W1094	W1095	W1096	W1097	W1098	W1099	W1100	W1101	W1102	W1103	W1104	W1105	W1106	W1107	W1108	W1109	W1110	W1111	W1112	W1113	W1114	W1115	W1116	W1117	W1118	W1119	W1120	W1121	W1122	W1123	W1124	W1125	W1126	W1127	W1128	W1129	W1130	W1131	W1132	W1133	W1134	W1135	W1136	W1137	W1138	W1139	W1140	W1141	W1142	W1143	W1144	W1145	W1146	W1147	W1148	W1149	W1150	W1151	W1152	W1153	W1154	W1155	W1156	W1157	W1158	W1159	W1160	W1161	W1162	W1163	W1164	W1165	W1166	W1167	W1168	W1169	W1170	W1171	W1172	W1173	W1174	W1175	W1176	W1177	W1178	W1179	W1180	W1181	W1182	W1183	W1184	W1185	W1186	W1187	W1188	W1189	W1190	W1191	W1192	W1193	W1194	W1195	W1196	W1197	W1198	W1199	W1200	W1201	W1202	W1203	W1204	W1205	W1206	W1207	W1208	W1209	W1210	W1211	W1212	W1213	W1214	W1215	W1216	W1217	W1218	W1219	W1220	W1221	W1222	W1223	W1224	W1225	W1226	W1227	W1228	W1229	W1230	W1231	W1232	W1233	W1234	W1235	W1236	W1237	W1238	W1239	W1240	W1241	W1242	W1243	W1244	W1245	W1246	W1247	W1248	W1249	W1250	W1251	W1252	W1253	W1254	W1255	W1256	W1257	W1258	W1259	W1260	W1261	W1262	W1263	W1264	W1265	W1266	W1267	W1268	W1269	W1270	W1271	W1272	W1273	W1274	W1275	W1276	W1277	W1278	W1279	W1280	W1281	W1282	W1283	W1284	W1285	W1286	W1287	W1288	W1289	W1290	W1291	W1292	W1293	W1294	W1295	W1296	W1297	W1298	W1299	W1300	W1301	W1302	W1303	W1304	W1305	W1306	W1307	W1308	W1309	W1310	W1311	W1312	W1313	W1314	W1315	W1316	W1317	W1318	W1319	W1320	W1321	W1322	W1323	W1324	W1325	W1326	W1327	W1328	W1329	W1330</
----	------	------	----	----	----	----	----	----	----	----	----	-----	-----	-----	-----	-----	-----	-----	-----	-----	-----	-----	-----	-----	-----	-----	-----	-----	-----	-----	-----	-----	-----	-----	-----	-----	-----	-----	-----	-----	-----	-----	-----	-----	-----	-----	-----	-----	-----	-----	-----	-----	-----	-----	-----	-----	-----	-----	-----	-----	-----	-----	-----	-----	-----	-----	-----	-----	-----	-----	-----	-----	-----	-----	-----	-----	-----	-----	-----	-----	-----	-----	-----	-----	-----	-----	-----	-----	-----	-----	-----	-----	-----	-----	-----	-----	-----	-----	-----	-----	-----	------	------	------	------	------	------	------	------	------	------	------	------	------	------	------	------	------	------	------	------	------	------	------	------	------	------	------	------	------	------	------	------	------	------	------	------	------	------	------	------	------	------	------	------	------	------	------	------	------	------	------	------	------	------	------	------	------	------	------	------	------	------	------	------	------	------	------	------	------	------	------	------	------	------	------	------	------	------	------	------	------	------	------	------	------	------	------	------	------	------	------	------	------	------	------	------	------	------	------	------	------	------	------	------	------	------	------	------	------	------	------	------	------	------	------	------	------	------	------	------	------	------	------	------	------	------	------	------	------	------	------	------	------	------	------	------	------	------	------	------	------	------	------	------	------	------	------	------	------	------	------	------	------	------	------	------	------	------	------	------	------	------	------	------	------	------	------	------	------	------	------	------	------	------	------	------	------	------	------	------	------	------	------	------	------	------	------	------	------	------	------	------	------	------	------	------	------	------	------	------	------	------	------	------	------	------	------	------	------	------	------	------	------	------	------	------	------	------	------	------	------	------	------	------	------	------	------	------	------	------	------	------	------	------	------	------	------	------	------	------	------	------	------	------	------	------	------	------	------	------	------	------	------	------	------	------	------	------	------	------	------	------	------	------	------	------	------	------	------	------	------	------	------	------	------	------	------	------	------	------	------	------	------	------	------	------	------	------	------	------	------	------	------	------	------	------	------	------	------	------	------	------	------	------	------	------	------	------	------	------	------	------	------	------	------	------	------	------	------	------	------	------	------	------	------	------	------	------	------	------	------	------	------	------	------	------	------	------	------	------	------	------	------	------	------	------	------	------	------	------	------	------	------	------	------	------	------	------	------	------	------	------	------	------	------	------	------	------	------	------	------	------	------	------	------	------	------	------	------	------	------	------	------	------	------	------	------	------	------	------	------	------	------	------	------	------	------	------	------	------	------	------	------	------	------	------	------	------	------	------	------	------	------	------	------	------	------	------	------	------	------	------	------	------	------	------	------	------	------	------	------	------	------	------	------	------	------	------	------	------	------	------	------	------	------	------	------	------	------	------	------	------	------	------	------	------	------	------	------	------	------	------	------	------	------	------	------	------	------	------	------	------	------	------	------	------	------	------	------	------	------	------	------	------	------	------	------	------	------	------	------	------	------	------	------	------	------	------	------	------	------	------	------	------	------	------	------	------	------	------	------	------	------	------	------	------	------	------	------	------	------	------	------	------	------	------	------	------	------	------	------	------	------	------	------	------	------	------	------	------	------	------	------	------	------	------	------	------	------	------	------	------	------	------	------	------	------	------	------	------	------	------	------	------	------	------	------	------	------	------	------	------	------	------	------	------	------	------	------	------	------	------	------	------	------	------	------	------	------	------	------	------	------	------	------	------	------	------	------	------	------	------	------	------	------	------	------	------	------	------	------	------	------	------	------	------	------	------	------	------	------	------	------	------	------	------	------	------	------	------	------	------	------	------	------	------	------	------	------	------	------	------	------	------	------	------	------	------	------	------	------	------	------	------	------	------	------	------	------	------	------	------	------	------	------	------	------	------	------	------	------	------	------	------	------	------	------	------	------	------	------	------	------	------	------	------	------	------	------	------	------	------	------	------	------	------	------	------	------	------	------	------	------	------	------	------	------	------	------	------	------	------	------	------	------	------	------	------	------	------	------	------	------	------	------	------	------	------	------	------	------	------	------	------	------	------	------	------	------	------	------	------	------	------	------	------	------	------	------	------	------	------	------	------	------	------	------	------	------	------	------	------	------	------	------	------	------	------	------	------	------	------	------	------	------	------	------	------	------	------	------	------	------	------	------	------	------	------	------	------	------	------	------	------	------	------	------	------	------	------	------	------	------	------	------	------	------	------	------	------	------	------	------	------	------	------	------	------	------	------	------	------	------	------	------	------	------	------	------	------	------	------	------	------	------	------	------	------	------	------	------	------	------	------	------	------	------	------	------	------	------	------	------	------	------	------	------	------	------	------	------	------	------	------	------	------	------	------	------	------	------	------	------	------	------	------	------	------	------	------	------	------	------	------	------	------	------	------	------	------	------	------	------	------	------	------	------	------	------	------	-------	-------	-------	-------	-------	-------	-------	-------	-------	-------	-------	-------	-------	-------	-------	-------	-------	-------	-------	-------	-------	-------	-------	-------	-------	-------	-------	-------	-------	-------	-------	-------	-------	-------	-------	-------	-------	-------	-------	-------	-------	-------	-------	-------	-------	-------	-------	-------	-------	-------	-------	-------	-------	-------	-------	-------	-------	-------	-------	-------	-------	-------	-------	-------	-------	-------	-------	-------	-------	-------	-------	-------	-------	-------	-------	-------	-------	-------	-------	-------	-------	-------	-------	-------	-------	-------	-------	-------	-------	-------	-------	-------	-------	-------	-------	-------	-------	-------	-------	-------	-------	-------	-------	-------	-------	-------	-------	-------	-------	-------	-------	-------	-------	-------	-------	-------	-------	-------	-------	-------	-------	-------	-------	-------	-------	-------	-------	-------	-------	-------	-------	-------	-------	-------	-------	-------	-------	-------	-------	-------	-------	-------	-------	-------	-------	-------	-------	-------	-------	-------	-------	-------	-------	-------	-------	-------	-------	-------	-------	-------	-------	-------	-------	-------	-------	-------	-------	-------	-------	-------	-------	-------	-------	-------	-------	-------	-------	-------	-------	-------	-------	-------	-------	-------	-------	-------	-------	-------	-------	-------	-------	-------	-------	-------	-------	-------	-------	-------	-------	-------	-------	-------	-------	-------	-------	-------	-------	-------	-------	-------	-------	-------	-------	-------	-------	-------	-------	-------	-------	-------	-------	-------	-------	-------	-------	-------	-------	-------	-------	-------	-------	-------	-------	-------	-------	-------	-------	-------	-------	-------	-------	-------	-------	-------	-------	-------	-------	-------	-------	-------	-------	-------	-------	-------	-------	-------	-------	-------	-------	-------	-------	-------	-------	-------	-------	-------	-------	-------	-------	-------	-------	-------	-------	-------	-------	-------	-------	-------	-------	-------	-------	-------	-------	-------	-------	-------	-------	-------	-------	-------	-------	-------	-------	-------	-------	-------	-------	-------	-------	-------	-------	-------	-------	-------	-------	-------	-------	-------	-------	-------	-------	-------	-------	-------	-------	-------	-------	-------	-------	-------	-------	-------	-------	-------	-------	-------	-------	-------	-------	-------	---------

Appendix C: Light curve parameters

Table C.1: Light curve parameters from SALT3 (t_0, x_0, x_1, c), SNooPy ($t_{max}, s_{BV}, E(B - V)_{host}$) and BayeSN (Peak $_{MID}, \mu$) along with peak apparent magnitudes in BJH . The errors are in the parentheses.

SN	SNCosmo					SNooPy					BayeSN				
	t_0	$x_0 \cdot 100\mu$	x_1	c	B_{max}	J_{max}	H_{max}	s_{BV}	$E(B - V)_{host}$	B_{max}	J_{max}	H_{max}	Peak $_{MID}$	μ	H_{max}
2018rw	58163.51 (0.25)	0.54 (0.02)	0.47 (0.17)	0.50 (0.02)	18.99 (0.04)	-	-	0.52 (0.06)	-0.02 (0.11)	18.98 (0.13)	-	-	58158.59 (0.91)	36.41 (0.95)	18.26 (0.10)
2018yu	58194.86 (0.04)	75.72 (1.23)	-0.16 (0.06)	-0.11 (0.01)	13.98 (0.02)	14.53 (0.02)	14.68 (0.02)	1.01 (0.04)	-0.04 (0.07)	14.02 (0.08)	14.36 (0.15)	14.79 (0.22)	58196.17 (0.26)	32.83 (0.26)	14.07 (0.04)
2018agk	58203.96 (0.11)	3.33 (0.10)	-1.27 (0.21)	-0.06 (0.02)	16.93 (0.03)	17.64 (0.03)	17.85 (0.03)	0.90 (0.06)	-0.49 (0.11)	18.25 (0.07)	17.08 (0.15)	17.07 (0.11)	58203.89 (0.51)	35.51 (0.53)	17.33 (0.12)
2018aog	58221.93 (0.10)	99.82 (0.83)	-1.49 (0.06)	-0.13 (0.01)	12.82 (0.02)	13.64 (0.02)	13.81 (0.02)	0.85 (0.03)	-0.05 (0.06)	12.85 (0.04)	13.20 (0.13)	13.65 (0.09)	58223.18 (0.15)	31.71 (0.15)	12.92 (0.02)
2018ayz	58238.85 (0.12)	0.65 (0.02)	-0.58 (0.15)	0.67 (0.01)	18.78 (0.10)	-	-	1.12 (0.04)	-0.38 (0.07)	17.21 (0.14)	16.97 (0.32)	16.62 (0.49)	58237.74 (0.34)	35.99 (0.35)	17.54 (0.05)
2018bie	58265.66 (0.02)	7.38 (0.05)	1.06 (0.03)	0.02 (0.01)	16.05 (0.01)	16.51 (0.01)	16.73 (0.01)	1.12 (0.04)	0.13 (0.06)	16.03 (0.02)	16.39 (0.05)	16.24 (0.14)	58265.32 (0.35)	34.95 (0.36)	15.94 (0.03)
2018bia	58263.35 (0.22)	16.34 (0.02)	0.39 (0.08)	0.12 (0.01)	15.58 (0.01)	15.47 (0.01)	15.63 (0.01)	0.61 (0.05)	-0.04 (0.09)	15.36 (0.06)	14.98 (0.13)	15.24 (0.14)	58267.00 (0.31)	33.51 (0.31)	15.55 (0.03)
2018caw	-	-	-	-	-	-	-	-	-	-	-	-	-	-	-
2018dda	58314.28 (0.18)	9.41 (0.14)	-0.19 (0.10)	0.17 (0.01)	15.85 (0.02)	15.83 (0.02)	16.03 (0.02)	1.19 (0.04)	0.17 (0.07)	15.79 (0.07)	15.49 (0.26)	16.49 (0.43)	58312.52 (0.23)	34.21 (0.23)	15.61 (0.02)
2018ebu	-	-	-	-	-	-	-	0.95 (0.07)	-0.15 (0.08)	17.98 (0.12)	-	-	58318.21 (8.60)	38.03 (9.13)	18.11 (0.05)
2018enc	58345.60 (0.05)	10.00 (0.07)	1.98 (0.07)	-0.09 (0.01)	16.04 (0.01)	16.55 (0.01)	16.76 (0.01)	1.32 (0.05)	-0.15 (0.07)	16.12 (0.03)	16.30 (0.07)	16.78 (0.07)	58346.18 (0.29)	35.01 (0.30)	16.04 (0.02)
2018ew	58342.43 (0.09)	23.16 (0.30)	-1.93 (0.19)	-0.16 (0.01)	15.47 (0.01)	15.99 (0.01)	16.14 (0.01)	0.68 (0.06)	-0.26 (0.11)	15.67 (0.08)	15.71 (0.08)	15.72 (0.12)	58341.45 (0.18)	34.46 (0.19)	15.59 (0.03)
2018evt	-	-	-	-	-	-	-	-	-	-	-	-	-	-	-
2018f	58354.18 (0.04)	6.45 (0.08)	0.18 (0.08)	-0.29 (0.01)	16.17 (0.01)	17.44 (0.01)	17.74 (0.01)	1.12 (0.05)	-0.20 (0.08)	16.39 (0.05)	17.35 (0.22)	17.79 (0.20)	58353.16 (0.20)	36.32 (0.21)	16.36 (0.04)
2018exb	58355.66 (0.07)	6.32 (0.01)	1.34 (0.10)	-0.13 (0.01)	16.22 (0.02)	16.98 (0.02)	-	1.09 (0.05)	-0.03 (0.07)	16.27 (0.07)	17.30 (0.17)	-	58354.37 (0.34)	35.61 (0.36)	16.16 (0.04)
2018eq	-	-	-	-	-	-	-	-	-	-	-	-	-	-	-
2018fcp	58406.97 (0.07)	5.48 (0.37)	0.173 (0.44)	0.04 (0.01)	16.55 (0.01)	16.82 (0.01)	17.02 (0.01)	0.88 (0.04)	0.06 (0.07)	16.63 (0.09)	16.67 (0.21)	18.77 (0.13)	58405.37 (0.21)	35.62 (0.21)	16.54 (0.02)
2018hgc	58412.96 (0.07)	2.61 (0.02)	-0.01 (0.05)	0.05 (0.01)	17.21 (0.01)	17.46 (0.01)	17.70 (0.01)	1.19 (0.04)	0.17 (0.07)	17.39 (0.04)	17.32 (0.20)	17.61 (0.13)	58412.50 (0.29)	36.05 (0.31)	17.15 (0.03)
2018hnn	58417.52 (0.04)	5.54 (0.06)	0.56 (0.05)	-0.07 (0.01)	17.09 (0.01)	17.31 (0.01)	-	1.12 (0.05)	0.02 (0.07)	16.59 (0.04)	16.77 (0.09)	-	58416.75 (0.28)	35.49 (0.29)	16.50 (0.04)
2018hvw	58412.55 (0.01)	3.48 (0.08)	-0.40 (0.11)	0.08 (0.01)	16.87 (0.02)	17.09 (0.02)	17.31 (0.02)	1.19 (0.04)	-0.04 (0.08)	16.19 (0.08)	18.07 (0.46)	17.49 (0.22)	58414.87 (0.07)	35.64 (0.08)	15.97 (0.05)
2018i	58450.58 (0.02)	15.07 (0.10)	0.73 (0.03)	-0.06 (0.01)	15.42 (0.01)	16.05 (0.01)	16.24 (0.01)	1.08 (0.03)	-0.01 (0.06)	15.45 (0.01)	15.75 (0.03)	16.20 (0.04)	58499.87 (0.20)	34.43 (0.20)	15.41 (0.02)
2018ig	58458.56 (0.72)	0.40 (0.72)	1.20 (1.90)	0.63 (0.08)	16.55 (0.20)	16.82 (0.20)	17.02 (0.20)	0.73 (0.04)	0.09 (0.11)	18.25 (0.17)	16.95 (0.24)	15.90 (0.21)	58453.41 (0.35)	35.99 (0.37)	17.90 (0.09)
2018jy	58468.71 (0.02)	14.55 (0.09)	-2.45 (0.02)	0.01 (0.01)	15.39 (0.01)	15.88 (0.01)	16.05 (0.01)	0.73 (0.03)	0.05 (0.06)	15.46 (0.01)	15.50 (0.27)	15.50 (0.21)	58467.36 (0.14)	34.08 (0.14)	15.45 (0.02)
2019fi	58499.11 (0.12)	1.19 (0.02)	1.06 (0.07)	-0.07 (0.01)	16.55 (0.02)	16.82 (0.02)	17.02 (0.02)	1.03 (0.04)	0.01 (0.06)	18.09 (0.02)	18.79 (0.17)	18.85 (0.12)	58498.60 (0.29)	37.26 (0.29)	17.90 (0.02)
2019fj	58501.48 (0.03)	1.77 (0.01)	-2.00 (0.03)	0.02 (0.01)	17.66 (0.01)	18.04 (0.01)	-	0.78 (0.03)	0.11 (0.06)	17.69 (0.02)	18.99 (0.19)	-	58501.45 (0.18)	36.28 (0.19)	17.62 (0.02)
2019fm	58503.14 (0.16)	9.17 (0.11)	0.59 (0.07)	0.01 (0.02)	16.15 (0.01)	16.38 (0.01)	16.56 (0.01)	0.45 (0.04)	0.01 (0.07)	15.94 (0.03)	16.90 (0.24)	16.19 (0.14)	58503.92 (0.37)	34.78 (0.37)	15.99 (0.04)
2019fo	58507.09 (0.02)	2.91 (0.16)	-1.66 (0.23)	0.18 (0.01)	17.51 (0.01)	17.21 (0.01)	17.34 (0.01)	0.45 (0.04)	0.01 (0.07)	17.19 (0.03)	16.10 (0.11)	16.18 (0.08)	58507.40 (0.12)	34.15 (0.13)	17.18 (0.02)
2019gh	58526.43 (0.08)	3.67 (0.07)	1.14 (0.09)	0.13 (0.01)	16.88 (0.02)	16.96 (0.02)	17.16 (0.02)	1.11 (0.05)	0.19 (0.07)	16.72 (0.09)	16.69 (0.09)	16.84 (0.12)	58525.45 (0.31)	35.35 (0.32)	16.69 (0.04)
2019agk	58528.61 (0.07)	2.09 (0.04)	1.43 (0.12)	-0.26 (0.01)	17.43 (0.02)	18.62 (0.02)	18.91 (0.02)	1.16 (0.06)	0.06 (0.10)	17.60 (0.11)	17.74 (0.75)	18.28 (0.68)	58528.89 (0.22)	36.87 (0.23)	17.47 (0.04)
2019awq	58539.96 (0.06)	2.61 (0.03)	-0.07 (0.07)	0.13 (0.01)	17.27 (0.01)	17.28 (0.01)	17.49 (0.01)	1.19 (0.05)	0.23 (0.07)	17.23 (0.03)	16.71 (0.17)	17.25 (0.10)	58540.03 (0.33)	35.58 (0.34)	17.18 (0.02)
2019bdz	58550.21 (0.05)	3.77 (0.02)	-0.72 (0.03)	-0.16 (0.01)	16.78 (0.01)	17.74 (0.01)	17.99 (0.01)	0.92 (0.03)	-0.04 (0.06)	16.79 (0.02)	17.95 (0.28)	17.93 (0.15)	58552.13 (0.23)	36.08 (0.24)	16.78 (0.02)
2019bus	58569.40 (0.17)	0.65 (0.01)	1.97 (0.19)	-0.06 (0.01)	18.66 (0.03)	-	-	1.22 (0.04)	-0.05 (0.07)	18.64 (0.07)	-	-	58568.61 (0.33)	37.91 (0.36)	18.31 (0.04)
2019cvi	58586.03 (0.07)	8.27 (0.06)	0.27 (0.07)	-0.06 (0.01)	16.30 (0.01)	16.70 (0.01)	16.89 (0.01)	0.97 (0.04)	0.04 (0.06)	16.25 (0.01)	16.39 (0.07)	16.86 (0.14)	58586.24 (0.35)	35.05 (0.36)	16.24 (0.02)
2019cxu	58586.35 (0.28)	0.55 (0.02)	-1.73 (0.40)	0.37 (0.03)	18.80 (0.05)	-	-	0.98 (0.03)	0.05 (0.06)	16.11 (0.04)	16.85 (0.23)	17.15 (0.10)	58593.77 (0.26)	35.25 (0.26)	16.11 (0.04)
2019czz	58593.66 (0.03)	6.76 (0.06)	-0.14 (0.04)	-0.08 (0.01)	16.12 (0.01)	16.90 (0.01)	17.13 (0.01)	1.00 (0.04)	-0.01 (0.06)	16.11 (0.04)	16.85 (0.23)	17.15 (0.10)	58599.07 (0.39)	36.86 (0.41)	17.36 (0.02)
2019dks	58599.25 (0.08)	1.79 (0.01)	0.99 (0.10)	-0.10 (0.01)	17.53 (0.02)	-	-	1.06 (0.06)	-	-	-	-	-	-	-
2019ein	-	-	-	-	-	-	-	-	-	-	-	-	-	-	-
2019fcr	58627.88 (0.05)	1.03 (0.01)	-0.18 (0.06)	0.12 (0.01)	18.38 (0.01)	-	-	0.96 (0.03)	0.29 (0.06)	18.33 (0.01)	-	-	58628.00 (0.27)	36.69 (0.28)	18.26 (0.04)
2019fmr	58632.82 (0.10)	19.94 (3.21)	1.13 (0.08)	-3.45 (0.08)	14.86 (0.37)	16.75 (0.37)	17.04 (0.37)	1.28 (0.14)	-0.88 (0.46)	-	16.67 (0.30)	16.81 (0.29)	58632.25 (0.70)	35.16 (0.72)	15.78 (0.08)
2019gbr	58647.34 (0.01)	27.57 (0.01)	-2.03 (0.01)	-0.14 (0.01)	14.72 (0.01)	15.65 (0.01)	15.83 (0.01)	0.85 (0.03)	-0.01 (0.06)	14.68 (0.03)	15.22 (0.15)	15.69 (0.17)	58647.78 (0.13)	33.78 (0.13)	14.84 (0.05)
2019gwa	58652.14 (0.03)	1.69 (0.02)	-0.09 (0.03)	0.00 (0.01)	17.76 (0.01)	-	-	1.11 (0.04)	0.20 (0.06)	17.94 (0.03)	-	-	58651.78 (0.16)	36.73 (0.14)	17.87 (0.06)

(a) Notice that x_0 and its error have been multiplied by 10^3 .

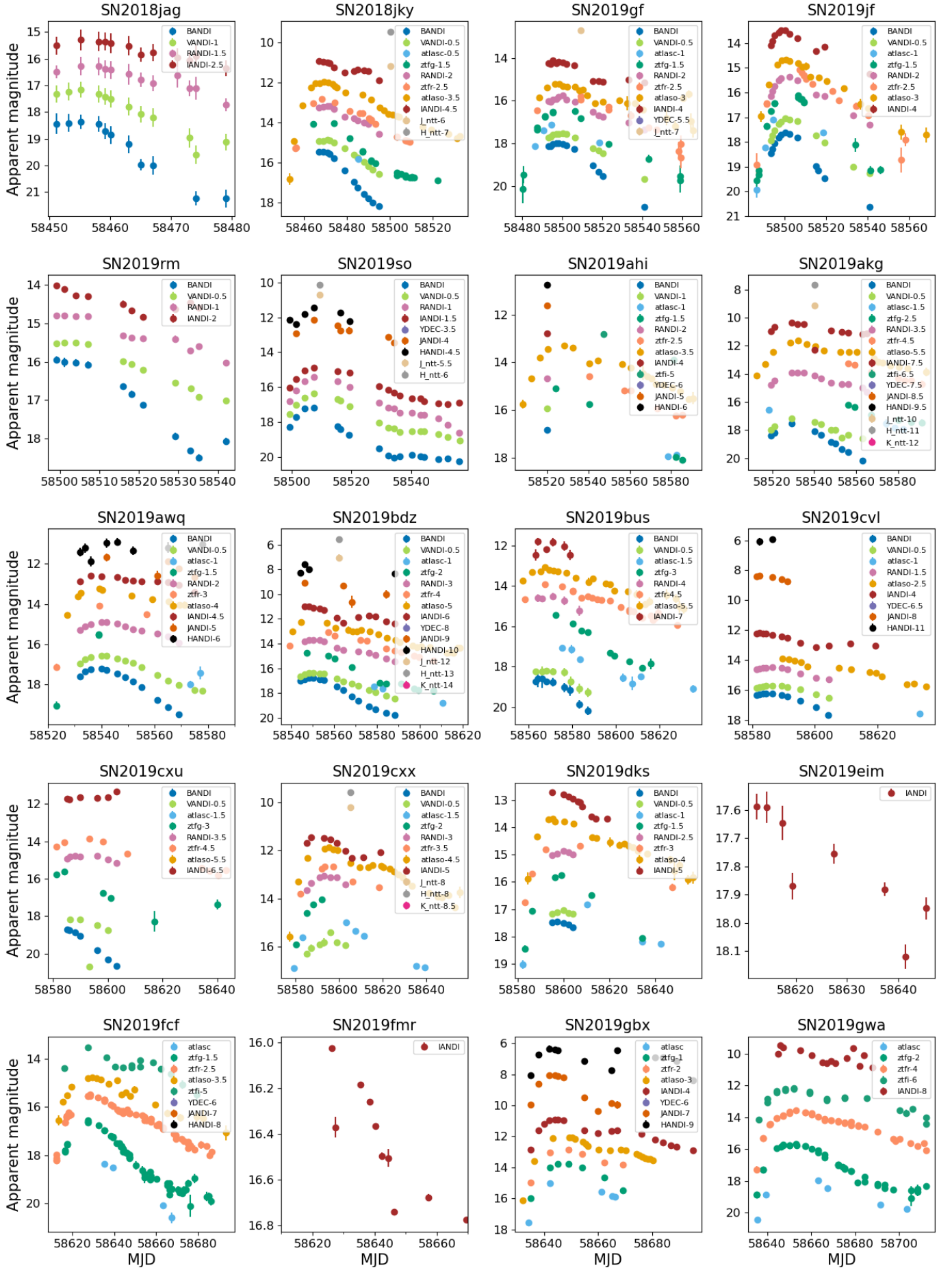


Fig. D.1: (cont.)

Appendix E: Light-curve fitting examples

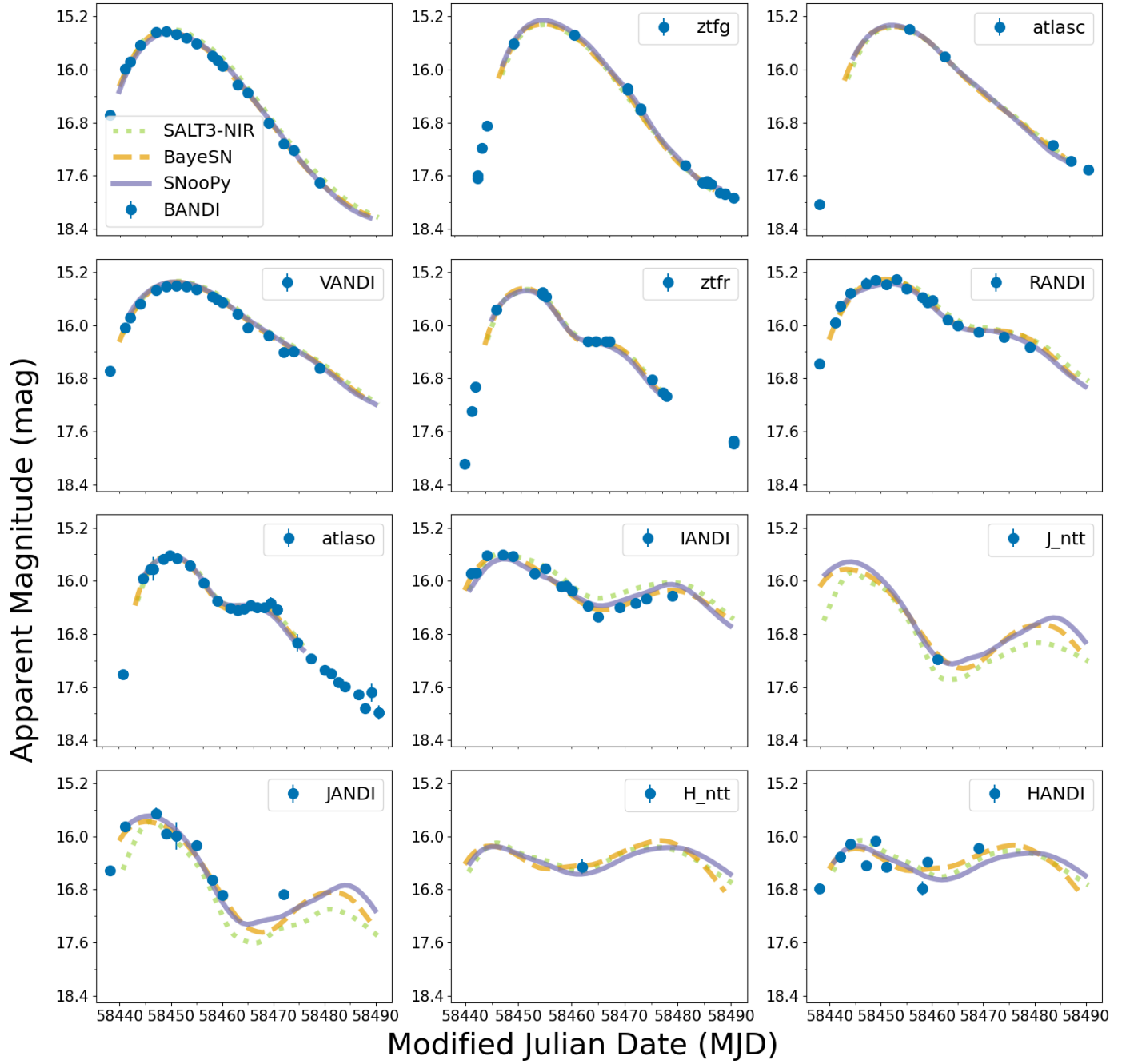


Fig. E.1: An example of light-curve fitting for SN 2018ilu in multiple filters using SALT3-NIR (green), BayeSN (orange), and SNooPy (purple).

Appendix F: Color terms

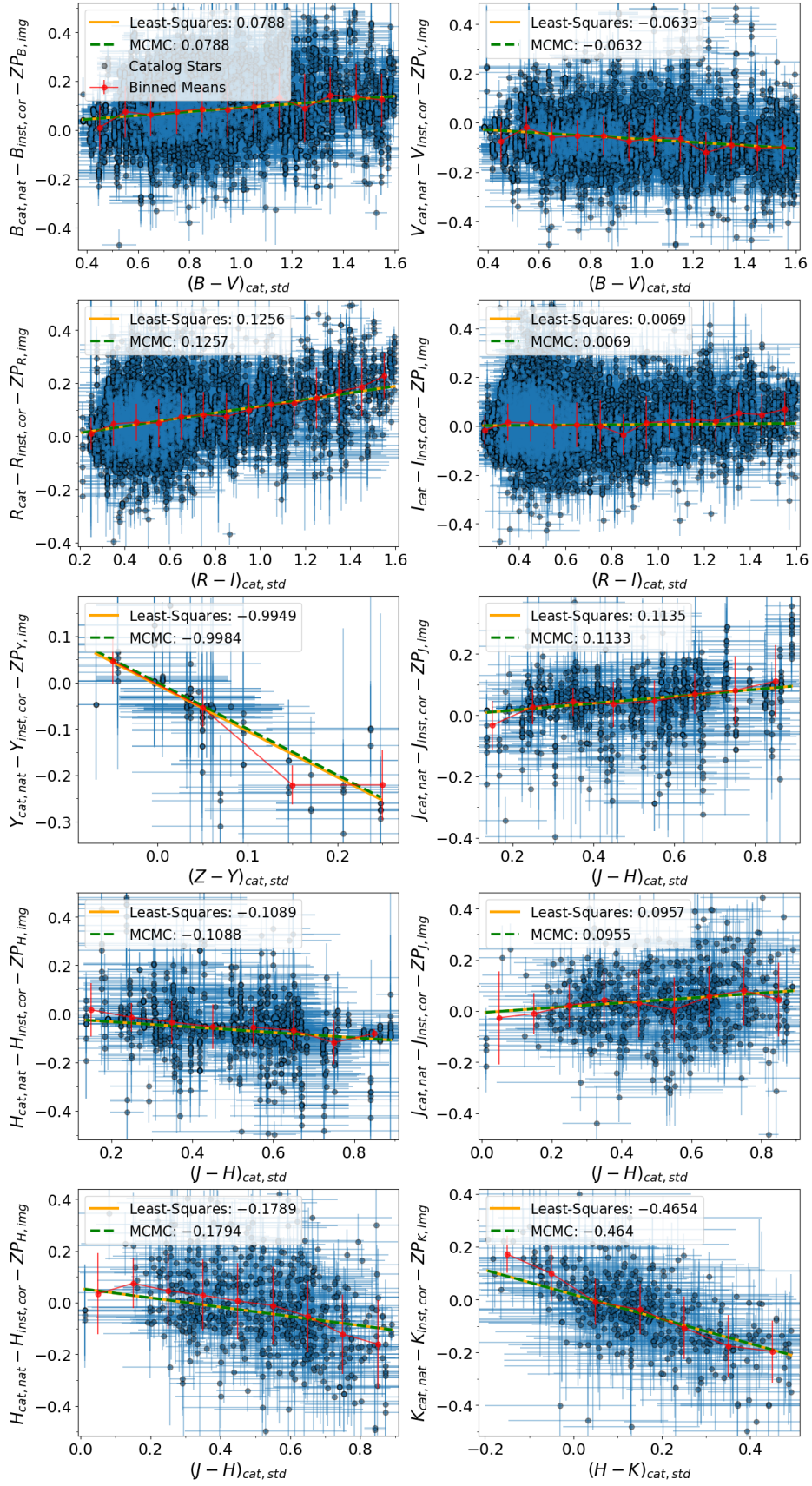


Fig. F.1: Same as Fig. 9, but for all ANDICAM and SOFI filters.